STRAIN TUNING THE NONRADIATIVE ENERGY TRANSFER RATE FROM QUANTUM DOTS TO WS_2

by

Esra Şimşek

B.S., Physics, Boğaziçi University,

2022

Submitted to the Institute for Graduate Studies in
Science and Engineering in partial fulfillment of
the requirements for the degree of
Master of Science

Graduate Program in Physics

Boğaziçi University

2024

ACKNOWLEDGEMENTS

I would like to express my gratitude to my supervisor, Assist. Prof. Burak Aslan, for his invaluable guidance throughout this journey.

I also want to extend my heartfelt thanks to my family, whose unwavering encouragement has been a constant source of strength. Especially to my sister Beyza—your support meant the world to me.

Most importantly, I am profoundly grateful to Oğuzhan, who has been my rock. You were with me every step of the way, and for that, I thank you.

I would also like to acknowledge the support received from TÜBİTAK Scientific and Technological Research Council of Turkey's (BİDEB) 2210-Domestic Graduate Scholarship Program, which was essential for the completion of this study.

ABSTRACT

STRAIN TUNING THE NONRADIATIVE ENERGY TRANSFER RATE FROM QUANTUM DOTS TO WS_2

This research investigates the effect of strain on the nonradiative energy transfer (NRET) rate between quantum dots (QDs) and bilayer (2L) WS_2, aiming to enhance our understanding of exciton dynamics in these hybrid systems. We initially calculated the NRET rate theoretically, expecting a decrease with increasing strain due to reduced overlap between the emission and absorption spectra. However, our experimental results showed the opposite trend. Time-resolved photoluminescence (TRPL) measurements revealed a decrease in exciton lifetime for QDs on 2L WS_2 under strain, indicating a more significant influence of nonradiative decay pathways, which was unexpected based on our theoretical calculations. Photoluminescence (PL) experiments under strain also showed a reduction in the integrated PL spectra, suggesting increased NRET efficiency with strain.

In addition to strain effects, we examined how the thickness of WS_2 influences NRET. TRPL measurements showed that the exciton lifetimes of QDs on 2L WS_2 (0.78 ns) and bulk WS_2 (2.64 ns) were shorter compared to QDs on PETG (3.24 ns), confirming that NRET is faster in 2L WS_2 than in bulk WS_2. These findings align with trends observed in existing literature.

Before addressing the discrepancies between theoretical predictions and experimental data, future studies should prioritize conducting additional experiments to validate our findings further.

ÖZET

GERİLİMİN KUANTUM NOKTALARINDAN WS_2'YE IŞINIMSIZ ENERJİ TRANSFERİ HIZINI DÜZENLEMESİ

Bu araştırma, hibrit sistemlerde eksiton dinamiklerini daha iyi anlamak amacıyla, kuantum noktaları (QD) ile iki-katmanlı (2L) WS_2 arasındaki ışınımsız enerji transferi (NRET) üzerine uygulanan gerilimin etkisini incelemektedir. Teorik olarak hesaplayarak, gerilim altında emisyon ve absorbsiyon spektrumları arasındaki örtüşmeyi azalacağını ve bu sebeple NRET'in azalacağını öngördük. Ancak, deneysel sonuçlarımız tam tersini gösterdi. Zaman çözünürlü fotolüminesans (TRPL) ölçümleri gerilim altında 2L WS_2 üzerindeki QD'ler için eksiton ömründe bir azalma olduğunu ortaya koydu, bu durum teorik hesaplamalarımıza göre beklenmedik bir şekilde ışınımsız bozulma yollarının daha büyük bir etkiye sahip olduğunu gösterdi. Gerilim altındaki fotolüminesans (PL) deneyleri de, toplam PL yoğunluğunda bir azalma olduğunu işaret ediyor, bu da gerilim ile NRET hızında bir artış olduğunu düşündürmektedir.

Gerilimin etkilerine ek olarak, WS_2 kalınlığının NRET'i nasıl etkilediğini de inceledik. TRPL ölçümleri, QD'lerin 2L WS_2 (0.78 ns) ve yığın WS_2 (2.64 ns) üzerindeki eksiton ömürlerinin, QD'lerin PETG üzerindeki ömürlerinden (3.24 ns) daha kısa olduğunu gösterdi, bu da NRET'in 2L WS_2'de yığın WS_2'ye göre daha hızlı gerçekleştiğini doğrulamaktadır. Bu bulgular, mevcut literatürde gözlemlenen sonuçlarla uyumludur.

Teorik tahminler ile deneysel veriler arasındaki uyumsuzluklara değinmeden önce, gelecekteki çalışmalar, bulgularımızı daha fazla doğrulamak için ek deneyler yapmaya odaklanmalıdır.

TABLE OF CONTENTS

ACKNOWLEDGEMENTS . . . iii
ABSTRACT . . . iv
ÖZET . . . v
LIST OF FIGURES . . . ix
LIST OF TABLES . . . xvii
LIST OF SYMBOLS . . . xviii
LIST OF ACRONYMS/ABBREVIATIONS . . . xix
1. INTRODUCTION . . . 1
1.1. Nonradiative Energy Transfer . . . 1
1.2. Transition Metal Dichalcogenides . . . 2
1.3. Quantum Dots . . . 4
1.4. Strain Engineering . . . 5
1.5. Material Choice . . . 7
1.5.1. WS_2 . . . 7
1.5.2. Choice of QD . . . 8
2. THEORY . . . 10
2.1. Gordon-Garstein Model . . . 10
2.2. Theoretically Calculating Strain Dependent NRET Rate from QD to 1L WS_2 . . . 12
2.2.1. Strain-Dependent $\epsilon(\omega)$ of 1L WS_2 . . . 12
2.2.2. Determining PL Spectrum and Size of the ZnCdSe/ZnSe Core-Shell QD . . . 14
2.2.3. Total NRET as a Function of Strain . . . 16
2.3. Kramers–Kronig Constrained Variational Analysis of Optical Spectrum 18
3. EXPERIMENTAL METHODS . . . 23
3.1. Mechanical Exfoliation . . . 23
3.1.1. Notes on Exfoliation . . . 24
3.2. Optical Measurements . . . 24

3.2.1. Setup . . . 25
3.2.2. Measurement Process . . . 26
3.2.3. Analysis of the Measurements . . . 26
3.2.3.1. PL Measurement Analysis . . . 26
3.2.3.2. Reflectance Measurement Analysis . . . 28
3.2.3.3. TRPL Measurement Analysis . . . 30
3.3. Dry Transfer of 2D Materials . . . 32
3.4. Strain Stage . . . 33
4. SUSPENDED WS_2 . . . 35
4.1. Samples on Holes . . . 35
4.2. Spin-Coating of QD . . . 37
4.2.1. Spin-Coating of Glass . . . 37
4.2.2. Spin-Coating of WS_2 Before Transfer (on PDMS) . . . 38
5. SUPPORTED WS_2 . . . 40
5.1. Tranfer of WS_2 to PETG Substrate . . . 40
5.2. Applying Strain to WS_2 . . . 42
5.3. Results . . . 47
6. STRAIN DEPENDENT NRET FROM QD TO WS_2 . . . 48
6.1. Coating the Surface with QD . . . 48
6.2. WS_2 on Top . . . 50
6.2.1. Strain-dependent PL Spectra of the QD . . . 52
6.3. QD on Top . . . 54
6.3.1. PL Measurements . . . 54
6.3.2. TRPL Measurements . . . 57
6.4. Results and Discussion . . . 59
7. THICKNESS DEPENDENT NRET FROM QD TO WS_2 . . . 61
7.1. TRPL Measurements . . . 61
7.2. PL Mapping . . . 61
7.3. Results and Discussion . . . 64
8. CONCLUSION . . . 66
REFERENCES . . . 68

APPENDIX A: FIGURE LICENCES 80

LIST OF FIGURES

Figure 1.1. Diagram showing the process of NRET, Γ_R represents the radiative decay and Γ_{NR} represent the nonradiative decay. 2

Figure 1.2. Crystal structures of single layers of transition metal dichalcogenides (TMDCs) in their trigonal prismatic (2H), octahedral (1T), and distorted octahedral (1T') phases. Lattice vectors and the stacking of atomic planes are indicated taken from [19]. 3

Figure 1.3. Calculated band structures of (a) MoS_2, (b) $MoSe_2$, (c) $MoTe_2$, (d) WS_2, and (e) WSe_2 from the bulk (upper panels) to 2L (middle panels) and 1L (bottom panels). The horizontal solid lines in each panel indicate the VBM, and the dotted lines indicate the CBM. The solid blue arrows indicate the lowest energy transitions, taken from [22]. 4

Figure 1.4. Size-dependent QD emission, taken from [27]. 5

Figure 1.5. PL spectra of 2L WSe_2 at different strain levels, PL spectra of unstrained 1L WSe_2 on SiO_2 is shown for comparison, taken from [45]. 6

Figure 1.6. Optical microscope image of a WS_2 crystal showing regions with varying layer thicknesses. 7

Figure 1.7. Emission spectra of: (a) ZnCdSe/ZnSe core-shell QD, (b) CdSe/ZnS core-shell QD with the imaginary part of in-plane dielectric function ($\mathrm{Im}[\epsilon_{\|}]$) of 1L/2L WS_2. 8

Figure 2.1. The structure of the GG model. 10

Figure 2.2. Experimentally obtained data taken from [61] and fit of (a) the imaginary and (b) the real part of the dielectric function of 1L WS_2. Dashed vertical lines indicate the peak energy of the *A, B, C, D* features [10]. 13

Figure 2.3. Calculated strain-dependent complex dielectric functions of 1L WS_2: (a) imaginary part, (b) real part [10]. 14

Figure 2.4. Gaussian fit to the PL spectrum of the QD. 15

Figure 2.5. (a) The image of QD under TEM, (b) the outlines of the selected QDs, (c) the histogram created using the areas outlined in the TEM images. 15

Figure 2.6. (a) Calculated NRET rate (normalized by Γ_0) from QD to 1L WS_2 for selected strain levels (1L graphene for comparison), (b) product of the normalized PL of QDs and the strain-dependent NRET rate [10]. 17

Figure 2.7. Total NRET rate between QD and 1L WS_2 as a function of strain [10]. 18

Figure 2.8. (a) Fitting Drude-Lorentz oscillators to Reflection Spectra of the 1L WS_2. (b) $\mathrm{Im}[\epsilon_{\parallel}]$, (c) and $\mathrm{Re}[\epsilon_{\parallel}]$ spectra of the 1L WS_2 obtained using KK-constrained variational analysis. 21

Figure 2.9. (a) $\mathrm{Im}[\epsilon_{\parallel}]$, (b) and $\mathrm{Re}[\epsilon_{\parallel}]$ spectra of the 1L and 2L WS_2 obtained using KK-constrained variational analysis compared with bulk WS_2. 21

Figure 2.10. (a) $\mathrm{Im}[\epsilon_{\parallel}]$, (b) and $\mathrm{Re}[\epsilon_{\parallel}]$ spectra of the 2-5L MoS_2 obtained using KK-constrained variational analysis compared with bulk MoS_2. . . 22

Figure 2.11. (a) Im[$\epsilon_{\|}$], (b) and Re[$\epsilon_{\|}$] spectra of the suspended 2L MoS_2 obtained using KK-constrained variational analysis compared with the 2L MoS_2 on PDMS. 22

Figure 3.1. Diagram showing the forces on the bulk crystal during exfoliation. 23

Figure 3.2. Result of difference between waiting time around: (a) one minute, (b) four minutes. 24

Figure 3.3. Diagram of the optical setup, same colored elements represent the same items. 25

Figure 3.4. (a) Subtraction of the substrate data (PETG) from the sample data, (b) interpolation of the substracted data with a given array. 27

Figure 3.5. Removing spikes from the interpolated data. 27

Figure 3.6. Setting a new baseline for the data. 28

Figure 3.7. (a) Collection efficiency of the setup, (b) efficiency corrected data, (c) peak analysis of the data. 28

Figure 3.8. Schematic of the reflectance measurement. 29

Figure 3.9. (a) The reflectance measurements from 1L WS_2, PDMS and the background, (b) reflection contrast spectrum of 1L WS_2 on PDMS substrate. 29

Figure 3.10. (a) Refractive index of PDMS n_{PDMS}, (b) reflection from PDMS R_{PDMS}. 30

Figure 3.11. Result of the fitting Lorentz oscillators to the exciton positions of the $R_{1L\ WS_2}$ 30

Figure 3.12. (a) Normalized data and IRF obtained from TRPL measurements, (b) deconvoluted data obtained from deconvolution of the TRPL data. 31

Figure 3.13. Result of the fitting exponential decay to the deconvoluted data. . 32

Figure 3.14. (a) Transfer setup, (b) close-up to the transfer setup. 33

Figure 3.15. Three-point bending strain apparatus: (a) initial design, (b) current state after filing to allow more space on top. 34

Figure 3.16. Schematic of the three-point bending apparatus and the flexible PETG substrate. 34

Figure 4.1. (a) Transfer of 2L WS_2 onto quartz substrate with hole, (b) PL spectra, (c) and $\Delta R/R_{\text{Quartz}}$ of 2L WS_2 on quartz substrate with hole. 36

Figure 4.2. (a) Diameter of the hole etched on the quartz substrate. Tear during the transfer of 2L WS_2 onto a hole: (b) Sample 15, (c) Sample 24. 36

Figure 4.3. (a) Spin-coating the QD onto a glass substrate, (b) PL from QD that is spin-coated onto the glass. 38

Figure 4.4. The surface of PDMS (a) before, (b) after spin-coating with toluene. 38

Figure 4.5. The surface of PDMS (a) before, (b) after spin-coating with ethanol. 39

Figure 5.1. Sample 33 on: (a) PDMS, (b) PETG after transfer. 41

Figure 5.2. Sample 37 on: (a) PDMS, (b) PETG after transfer. 41

Figure 5.3. PL spectra of Sample 33 with the clamp width of 37 mm, same colored spectra represent the same strain level. 42

Figure 5.4. Strain-dependent (a) linewidth, (b) peak energy analysis of the PL spectra of Sample 33 with the clamp width of 37 mm. 43

Figure 5.5. (a) PL spectra, (b) strain-dependent linewidth, (c) and peak energy analysis of the PL spectra of Sample 33 when the strain was applied the second time with the clamp width of 18 mm. 44

Figure 5.6. (a) Sample 33 after the strain applied, (b) PETG substrate after strain is applied. 44

Figure 5.7. (a) PL spectra, (b) strain-dependent linewidth, (c) and peak energy analysis of the PL spectra of Sample 37 with the clamp width of 21 mm. 45

Figure 5.8. (a) PL spectra, (b) strain-dependent linewidth, (c) and peak energy analysis of the PL spectra of Sample 37 when the strain was applied the second time with the clamp width of 19 mm. 46

Figure 6.1. PL spectrum of the CdSe/ZnS QD. 48

Figure 6.2. The surface of PETG: (a) bare, (b) ethanol dropped, (c) toluene dropped. 49

Figure 6.3. WS_2 flakes on PETG : (a,c) before, (b,d) after water is dropped. 49

Figure 6.4. (a) Dried QD on PETG, (b) reflected laser from outside the QD circle, (c) from the outline of the circle. 50

Figure 6.5. Sample 18 is on: (a) PDMS before the transfer, (b) on PETG after the transfer. 51

Figure 6.6. PL spectra of: (a) QD on PETG, (b) 1L WS_2 on QD, (c) 2L WS_2 on QD on Sample 18. 51

Figure 6.7. Strain-dependent integrated area of: (a) QD on PETG, (b) 1L WS_2 on QD, (c) 2L WS_2 on QD on Sample 18. 52

Figure 6.8. PL from: (a) Point 1, (b) Point 2. 53

Figure 6.9. Strain-dependent spectra of QD: (a) Point 1, (b) Point 2. 53

Figure 6.10. Strain-dependent integrated area of PL spectra: (a) Point 1, (b) Point 2. 54

Figure 6.11. Sample 27 on the PETG, double arrow shows the direction of the applied strain. 54

Figure 6.12. Strain-dependent PL spectra of QD on: (a) PETG, (b) 1L WS_2, (c) 2L WS_2 on Sample 27. 55

Figure 6.13. Strain-dependent integrated area under PL spectra of QD: on (a) PETG, (b) 1L WS_2, (c) 2L WS_2 on Sample 27. 56

Figure 6.14. Strain-dependent electric field intensity relative to the incident intensity on the surface of 2L WS_2 on PETG. 56

Figure 6.15. Sample 41 on PETG, double arrow shows the direction of the applied strain. 57

Figure 6.16. Different decays obtained with different noise power values to wiener deconvolution. 57

Figure 6.17. (a) Normalized count of the data taken from Sample 41, (b) deconvolution of the TRPL data together with normalized data for comparison. 58

Figure 6.18. Lifetimes obtained by making exponential fits to deconvoluted data as a function of strain. 58

Figure 6.19. Total NRET rate between CdSe/ZnS QD and 2L WS_2 as a function of strain. 59

Figure 7.1. Comparing the lifetime of the excitons in QD on PETG, 2L WS_2 and bulk WS_2 on Sample 41. 61

Figure 7.2. Sample 39 on PETG. 62

Figure 7.3. Heatmap of the integrated areas of the PL spectra of QD on: (a) PETG, (b) 2L WS_2. 62

Figure 7.4. Electric field intensity relative to the incident intensity on the surface of PETG and 2L WS_2, PL spectra of QD to compare. 63

Figure 7.5. Heatmap of the peak energy of the PL spectra of (a) QD on PETG, (b) QD on 2L WS_2. Heatmap of the linewidth of the PL spectra of (c) QD on PETG, (d) QD on 2L WS_2. 64

Figure 7.6. TRPL traces on graphene layers are shown in the top panel and on MoS_2 in the bottom panel. Exemplary fits are overlaid on the data in solid blue and red lines. The gray trace corresponds to the SiO_2 substrate, and the instrument response function is the dashed black line taken from [66]. 65

LIST OF TABLES

Table 1.1. Excitonic linewidth of the TMDCs at room temperature, taken from [56]. 8

Table 5.1. Investigated properties of the PETG sheets. 42

Table 5.2. Statistics of the strain applied to 1L WS_2. 47

LIST OF SYMBOLS

A	Ampere
c	Speed of light
E	Energy
eV	Electron volt
$\hbar$	Planck's constant/2π
meV	Millielectron volt
MHz	Megahertz
min	Minutes
mW	Milliwatt
nm	Nanometer
p	Dipole transition moment
s	Second
v	Velocity
k_e	Emission wavenumber
ϵ	Dielectric function
$\epsilon_{\parallel}$	In-plane dielectric function
$\epsilon_{\perp}$	Out-of-plane ielectric function
μm	Micrometer
ω	Angular frequency

LIST OF ACRONYMS/ABBREVIATIONS

0D	Zero Dimensional
1L	Monolayer
2D	Two Dimensional
2L	Bilayer
CBM	Conduction Band Minimum
Cd	Cadmium
$CdSe_2$	Cadmium Diselenide
FRET	Förster Resonance Energy Model
GG	Gordon-Garstein
KK	Kramers-Kronig
Mo	Molybdenum
MoS_2	Molybdenum Disulfide
$MoSe_2$	Molybdenum Diselenide
NRET	Nonradiative Energy Transfer
IRF	Instrument Response Function
PC	Polycarbonate
PDMS	Polydimethylsiloxane
PETG	Polyethylene Terephthalate glycol
PL	Photoluminescence
PMMA	Polymethyl methacrylate
rpm	Rotation per Minute
QD	Quantum Dot
S	Sulfur
Se	Selenium
TEM	Transmission Electron Microscopy
TMDC	Transitional Metal Dichalcogenide
TRPL	Time-Resolved Photoluminescence
VBM	Valance Band Maximum

VdW	Van der Waals
W	Tungsten
WS_2	Tungsten Disulfide
WSe_2	Tungsten Diselenide
Zn	Zinc

1. INTRODUCTION

Over the past decade, low-dimensional semiconductor materials have gained significant attention in electronic applications due to their distinctive properties, particularly their strong light-matter interactions. Quantum dots (QDs), known for their high quantum efficiencies and tunable band gaps, are valuable components in this context. However, their poor carrier transport properties pose a challenge compared to transition metal dichalcogenide (TMDC) crystals. A key aspect of optimizing these materials for optoelectronic performance lies in controlling their excitonic processes, such as nonradiative energy transfer (NRET). Thus, engineering NRET in hybrid nanostructures that combine QDs with TMDCs offers a promising pathway to enhance and better understand these interactions.

This thesis investigates the NRET from zero-dimensional (0D) QDs to two-dimensional (2D) tungsten disulfide (WS_2). This chapter provides background information on the materials and our approach to tuning the NRET rate. Chapter 2 delves into the theoretical foundation of our work and outlines the analytical methods employed. Chapter 3 introduces our experimental techniques, while Chapter 4 discusses the challenges encountered with suspended materials. In Chapter 5, we explain our choice of substrate. In Chapters 6 and 7, we present the tuning of NRET and analyze the experimental results. Finally, in Chapter 8, we discuss the results of the experiments and conclude the thesis.

1.1. Nonradiative Energy Transfer

In some systems, excited electron-hole pairs (excitons) are transferred without emission photons. This is due to near-field effects and can be understood as the quenching of the PL spectrum of the donor dipole in the presence of a lossy medium as Figure 1.1 illustrates. This interaction is also called NRET [1] and it is the primary process responsible for reducing the lifetime of excited states [2]. It has a crucial role in the

energy (or exciton) transfer [3] and is the prominent decay channel in short distances. The mechanism involves an energy donor and an accepting medium.

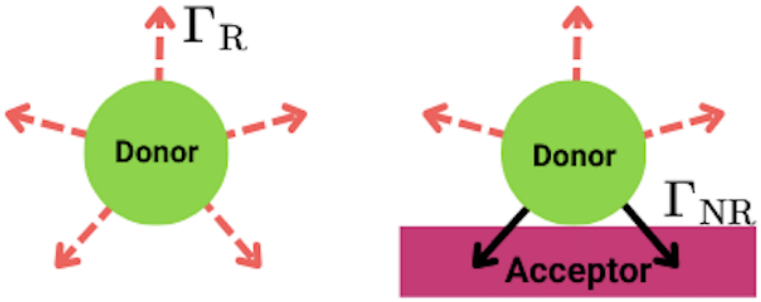

Figure 1.1. Diagram showing the process of NRET, Γ_R represents the radiative decay and Γ_{NR} represent the nonradiative decay.

In recent years, NRET has gained popularity for electronic and optic applications as an enabler/enhancer in the operation of various hybrid nanostructures [4–6]. Its efficiency is affected by the separation distance between the donor and the acceptor, making it a valuable tool for measuring the distance in biological systems [7] and in nanoscale sensors [8, 9]. The NRET rate also depends on the spectral overlap between donors' emission spectra and the acceptor's absorption spectra. Thus, engineering that overlap [10] can optimize it.

1.2. Transition Metal Dichalcogenides

Dimension of the material has an irrefutable impact on its optical, chemical, and electronic properties. The layered Van der Waals (VdW) "2D" materials have become popular ever since it was shown that isolated graphene can be obtained by exfoliation and is stable at room temperature and in the air while maintaining its macroscopic continuity and almost no effect on its carrier mobility [11]. Graphene's success as a 2D material paved the way for researchers to explore other 2D materials. TMDCs, common formula MX_2 (M = Mo, W; X = S, Se), are considered as one of these "other" 2D materials. Although Linus Pauling first determined their structure in the 1920s [12] and the production of thin film reports back to the 1960s [13], their rise in the field of

nanotechnology and materials coincides with the emergence of the graphane [14].

There are two common structural phases for TMDCs. These phases are characterized by either trigonal prismatic (2H) or octahedral (1T) coordination of metal atoms as illustrated in Figure 1.2. In their thermodynamically stable 2H phase, MoS_2, $MoSe_2$, WS_2 and WSe_2 are semiconductors and ideal for electronic applications [15–18].

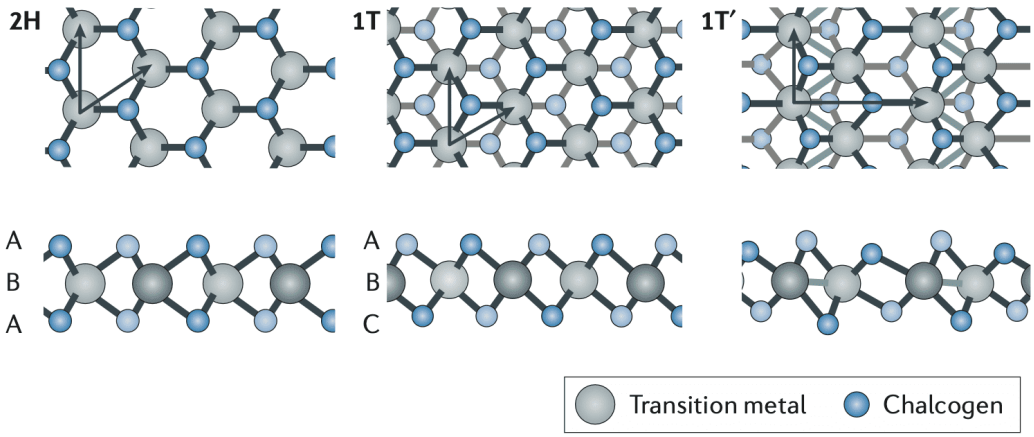

Figure 1.2. Crystal structures of single layers of transition metal dichalcogenides (TMDCs) in their trigonal prismatic (2H), octahedral (1T), and distorted octahedral (1T') phases. Lattice vectors and the stacking of atomic planes are indicated taken from [19].

The most distinct property of the TMDC is when thickness decreases, positions of the valence band maximum (VBM) and conduction band minimum (CBM) edges change. This change causes the indirect bandgap to become direct in the 1L limit, as shown in Figure 1.3. VBM and CBM of 1L 2H-TMDCs are located at the two inequivalent high-symmetry points K and K', corresponding to the corners of the hexagonal Brillouin zone. This property leads to observing valley-dependent physical phenomena and potential valleytronics applications. Furthermore, their lack of inversion symmetry causes a spin splitting of the electronic bands driven by the spin-orbit interaction [19]. Plus, the spin degeneracy of the VBM and CBM at K and K' points are lifted, also known as spin-valley coupling, because these points do not correspond to the time-reversal invariant momenta [20] making them ideal candidates for spintronics

devices [21].

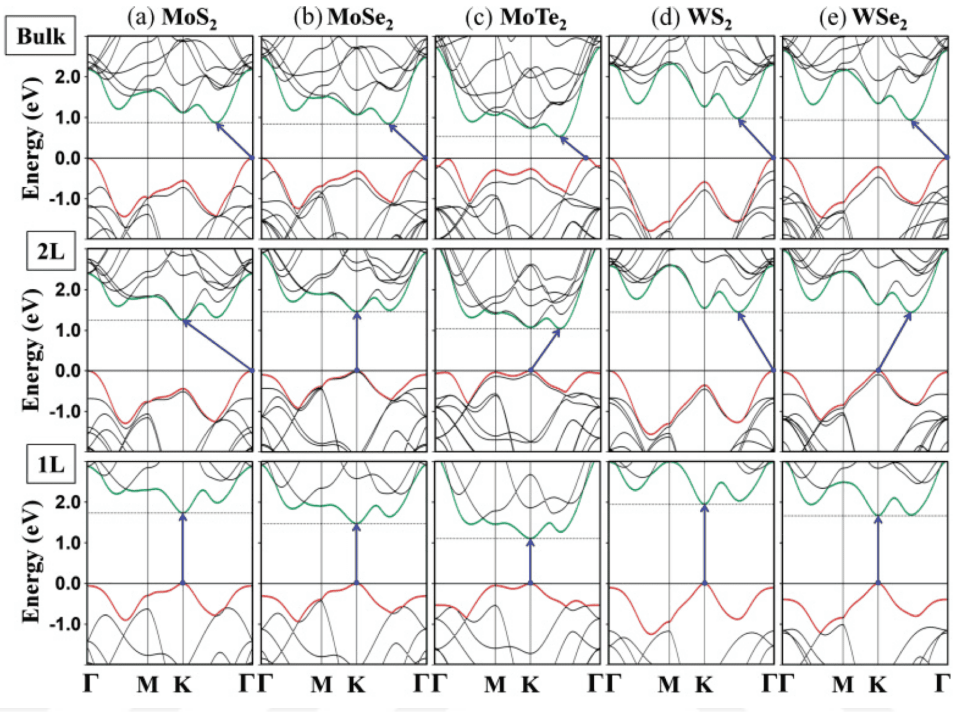

Figure 1.3. Calculated band structures of (a) MoS_2, (b) $MoSe_2$, (c) $MoTe_2$, (d) WS_2, and (e) WSe_2 from the bulk (upper panels) to 2L (middle panels) and 1L (bottom panels). The horizontal solid lines in each panel indicate the VBM, and the dotted lines indicate the CBM. The solid blue arrows indicate the lowest energy transitions, taken from [22].

1.3. Quantum Dots

Semiconductor's tunable optical and electronic properties offer a wide range of applications from medical [23, 24] to electronic [15], [25]. Combining two semiconductors with different bandgap energies and spatial dimensions confines the motion of electrons and holes, thus creating a single or periodic potential well. QDs result from combining two spherical semiconductors, forming a three-dimensional potential well at the nanometer scale [26].

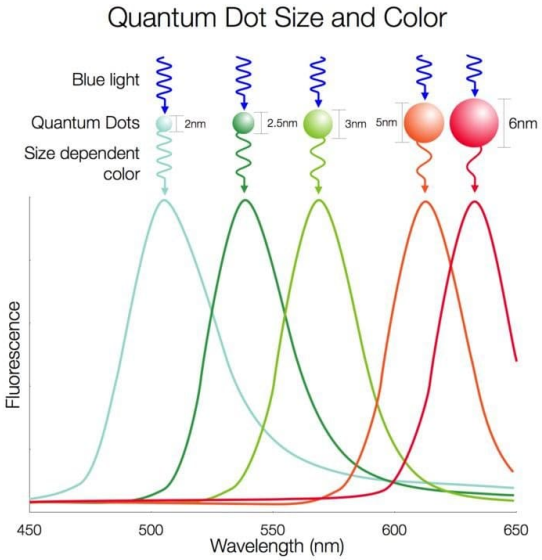

Figure 1.4. Size-dependent QD emission, taken from [27].

The physics of QDs is closer to classical physics than atomic physics, yet they are sufficiently small to exhibit quantum phenomena [28]. They have a discrete atom-like electronic structure and size-dependent energy levels because of the restricted electron motion [29]. For instance, the smallest CdSe nanocrystals with less than 2 nm diameter show blue fluorescence. In contrast, larger nanocrystals of the same material (diameter $\approx$ 6 nm) emit red light [30]. Figure 1.4 illustrates the different color peak emissions from the same QD with different radii.

1.4. Strain Engineering

By tuning optical and electronic properties, TMDCs can be optimized for specific applications, such as photovoltaics [31], photodetectors [32], and transistors [33]. Electrostatic gating [34, 35], chemical doping [36], or changing the dielectric environment (substrate/superstrate) [37, 38] are among the commonly used tuning methods for the TMDC. 2D materials can also be combined with specialized structures and materials like nanocavities, photonic crystals, and metamaterials to modify the interaction with light and even enable optical transitions that are typically not allowed [39, 40]. Of all the tuning methods available, we have chosen strain engineering as our means.

Strain engineering has gained significant attention in the literature due to its strong influence on the optoelectronic properties of TMDCs [41–43]. Unlike their bulk counterparts, 2D materials exhibit remarkable strength, allowing them to endure much higher levels of strain [44]. Researchs shows that strain manipulation offers several advantages over other tuning methods: it is dynamic, reversible, and capable of inducing more pronounced changes in 2D materials. The most distinct property of TMDCs under strain is the transformation of the indirect bandgap in 2L TMDCs into a direct bandgap similar to 1L TMDCs with an enhancement on their PL [45,46]. Additionally, strain tuning has a minimal impact on exciton binding energies and the energy gaps between excitons compared to other techniques [43].

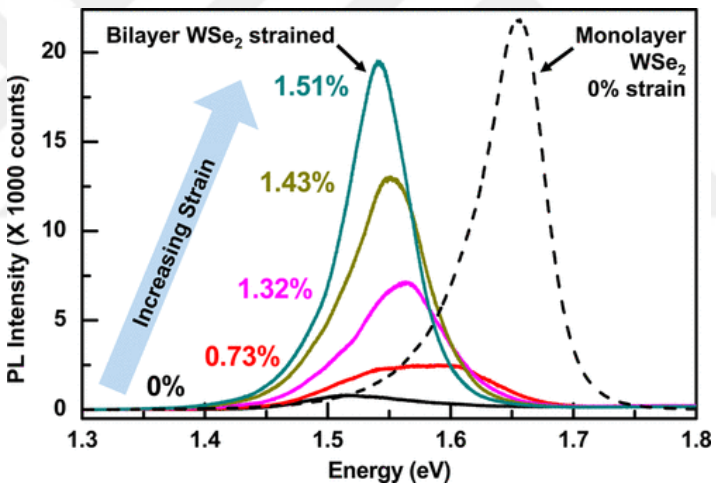

Figure 1.5. PL spectra of 2L WSe_2 at different strain levels, PL spectra of unstrained 1L WSe_2 on SiO_2 is shown for comparison, taken from [45].

Strain can be applied to TMDCs using different methods such as bending, pressure, and substrate engineering. Bending involves placing the TMDCs on flexible materials, such as PMMA [47] and PC [42], which can be bent or stretched to create strain in the material. This method allows for easy adjustment and reversal of strain [48]. Pressure application uses mechanical force or fluid pressure to compress the material, creating strain [49]. Substrate engineering is another approach, where TMDCs are placed on materials that expand or contract with temperature changes or are pre-stretched. As the substrate changes, it transfers strain to the TMDCs, allowing

for precise control of the strain [50]. A detailed explanation of our strain method and how we apply it is presented in Section 3.4.

1.5. Material Choice

We select core-shell QDs with spherical symmetry as our energy donors because they have a high PL yield, making it easy to detect any reduction in their PL. Additionally, their band-edge excitons have a long lifetime before recombination, allowing sufficient time for nonradiative energy transfer. For the acceptor, we use 1L/2L WS_2.

1.5.1. WS_2

Among TMDC, we focus on WS_2 for its unique characteristics such as high emission quantum yield [51], large exciton and trion binding energies [52] and a high room temperature mobility $\sim$100 $cm^2v^{-1}s^{-1}$ [53].

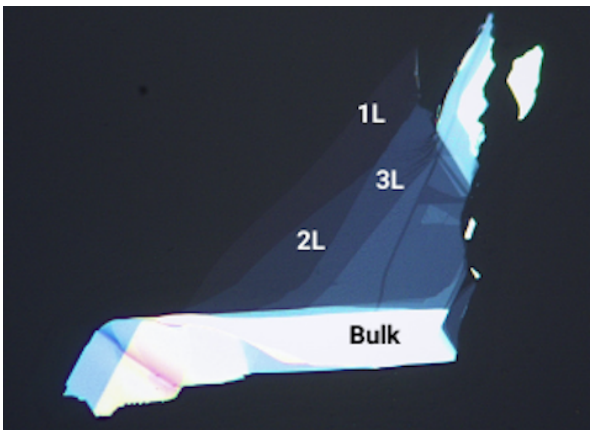

Figure 1.6. Optical microscope image of a WS_2 crystal showing regions with varying layer thicknesses.

WS_2 has a bandgap energy of around 2 eV in the 1L limit [54] and shows strong PL with visible light, even at room temperature [55]. When combined with its relatively sparse occurrence of defects, 1L WS_2 displays a greater PL quantum yield (approximately 6%) compared to other 2D semiconductors [51]. Furthermore, it has

the smallest A exciton linewidth and is also the least sensitive to strain [43]. Table 1.1 gives the details about the A exciton linewidth of the TMDCs under 1% uniaxial strain at room temperature.

Table 1.1. Excitonic linewidth of the TMDCs at room temperature, taken from [56].

Linewidth (meV)	WS_2	MoS_2	$MoSe_2$	WSe_2
Unstrained	19.48	51.31	56.85	38.57
1% Strain	11.21	66.60	51.97	18.89

All these remarkable properties combined with biexciton [57], single-photon emission [58], exciton-polaritons [59] and stimulated emission [60] in 1L WS_2, WS_2 holds great promise for advancements in next-generation nanoelectronics, optoelectronics, spintronics, and valleytronics applications.

1.5.2. Choice of QD

We chose ZnCdSe/ZnSe core-shell QD with radius r = 3.32 nm and CdSe/ZnS core-shell QD with radius r ≈ 4 nm since their emission spectra coincide with 1L/2L WS_2 absorption spectra as shown in Figure 1.7.

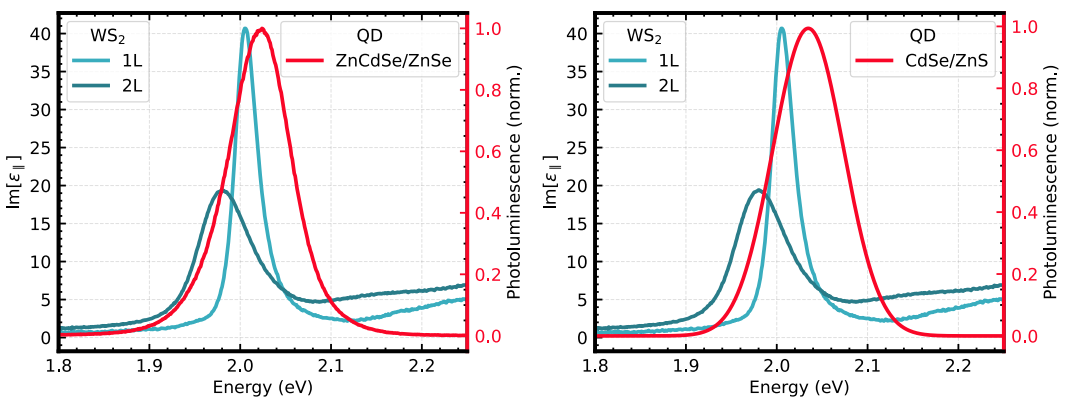

(a) (b)

Figure 1.7. Emission spectra of: (a) ZnCdSe/ZnSe core-shell QD, (b) CdSe/ZnS core-shell QD with the imaginary part of in-plane dielectric function ($\mathrm{Im}[\epsilon_{\parallel}]$) of 1L/2L WS_2.

In the Figure 1.7, we used $\mathrm{Im}[\epsilon_{\|}]$ to represent absorption spectra since it is proportional to the absorption coefficient [61].

2. THEORY

This chapter focuses on the underlying principles behind the modeling of the NRET and computes the strain-dependent NRET from QDs to 1L WS_2. Additionally, the chapter discusses the Kramers-Kronig constrained variational analysis, a valuable tool for calculating the dielectric function of a material from its reflection spectrum.

2.1. Gordon-Garstein Model

There are various models to describe NRET. The Förster resonance energy transfer (FRET) model is the most popular [62, 63]. However, in the FRET model, the transfer rate has a $1/r^6$ dependence on the separation distance [2], and it ignores the dipole-dipole interaction in the accepting medium and underestimates the dielectric screening effect within the material [64].

In this section, we follow the macroscopic model that Gordon and Garstein (GG) utilize [65]. In this model, the acceptor slab is treated as a continuum characterized by its frequency-dependent dielectric function $\epsilon(\omega) = \epsilon_1(\omega) + i\epsilon_2(\omega)$ and energy donor species is represented by a standard electric point-like dipole emitter with the (effective) dipole transition moment $\mathbf{p}$.

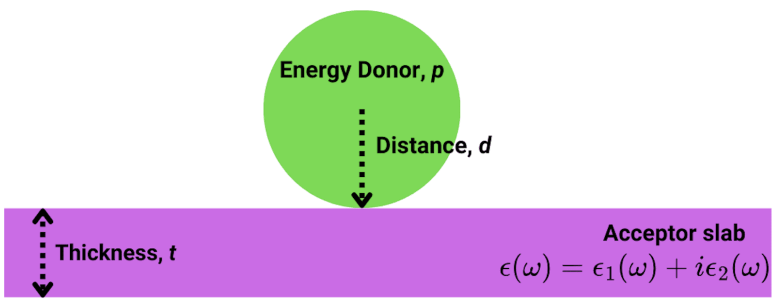

Figure 2.1. The structure of the GG model.

The dipole experiences a spontaneous (radiative) decay rate in the vacuum

$$\Gamma_0 = \frac{4k_e^3|\mathbf{p}|^2}{3\hbar}, \tag{2.1}$$

where $k_e = \omega/c$ emission wave number. In our calculations, we replace k_e with energy using $k_e = E/\hbar c$.

In the electrostatic limit (c $\to \infty$), NRET rate Γ, normalized with the spontaneous emission to the vacuum Γ_0, for an isotropic slab takes the form

$$\frac{\Gamma}{\Gamma_0} = \frac{3(\hbar c)^3}{2(Ed)^3} \times Im\left[\int_0^\infty d\rho\rho^2 e^{-2\rho} \times \frac{(\epsilon^2-1)(1-e^{-2\rho t/d})}{(\epsilon+1)^2-(\epsilon-1)^2 e^{-2\rho t/d}}\right], \tag{2.2}$$

where d is the distance between the center of the dipole and the surface of the acceptor, t is the thickness of the acceptor whose dielectric properties as defined by $\epsilon(\omega)$ and ρ is the integral variable. The model's calculations are limited to the donor transition moment perpendicular to the free-standing slab.

We prefer to normalize Γ with Γ_0 since we work with thin materials. When investigating the Γ into bulk/thick material (where $t/d \to \infty$, semispace), choosing to normalize using the formula for Γ^∞

$$\frac{\Gamma^\infty}{\Gamma_0} = \frac{3\epsilon_2(\hbar c)^3}{4(Ed)^3|\epsilon+1|^2}, \tag{2.3}$$

is better.

When the acceptor slab is anisotropic, Equation (2.2) takes the form

$$\frac{\Gamma}{\Gamma_0} = \frac{3(\hbar c)^3}{2(Ed)^3} \times Im\left[\int_0^\infty d\rho\rho^2 e^{-2\rho} \times \frac{(\beta^2-1)(1-e^{-2\rho\delta t/d})}{(\beta+1)^2-(\beta-1)^2 e^{-2\rho\delta t/d}}\right], \tag{2.4}$$

where $\beta = \sqrt{\epsilon_\parallel \epsilon_\perp}$ (effective permittivity of the acceptor) and $\delta = \sqrt{\epsilon_\parallel/\epsilon_\perp}$ (dielectric anisotropy of the acceptor). $\epsilon_\parallel, \epsilon_\perp$ represent the in and out-of-plane dielectric functions,

respectively.

We like to mention that, in the GG model, the absorber is a free-standing slab, meaning that the model assumes the material is suspended. However, unlike the GG model, we use PETG as a substrate in our experiments. When we investigated the literature to see whether we needed to change our model, we saw that the same model had been used when performing experiments with substrates [63], [66], and using substrate only changes the result quantitatively.

The quantitative difference between suspended and supported material varies for different materials. For instance, the NRET rate from QD to graphene on a substrate is lower than into the vacuum, whereas for MoS_2 with substrate, it is increased [66]. This could be explained by the effect of substrate on material absorption and screening ability. TMDC's absorption on fused silica is decreased compared to free standing [61].

2.2. Theoretically Calculating Strain Dependent NRET Rate from QD to 1L WS_2

2.2.1. Strain-Dependent $\epsilon(\omega)$ of 1L WS_2

We model $\epsilon_{\|}$ as a superposition of four Lorentz-Drude Oscillators

$$\epsilon_{\|}(E) = \epsilon_b + \sum_{m=1}^{4} \frac{f_m}{E_m^2 - E^2 - iE\gamma_m}, \tag{2.5}$$

where f_m is the oscillator strength, γ_m is the linewidth, and E_m is the resonance energy of the mth oscillator. ϵ_b is the background dielectric constant representing the contribution of the higher energy resonances, which are not included in our model. In Equation (2.5) each oscillator corresponds to an exciton position, *A, B, C* and *D* respectively.

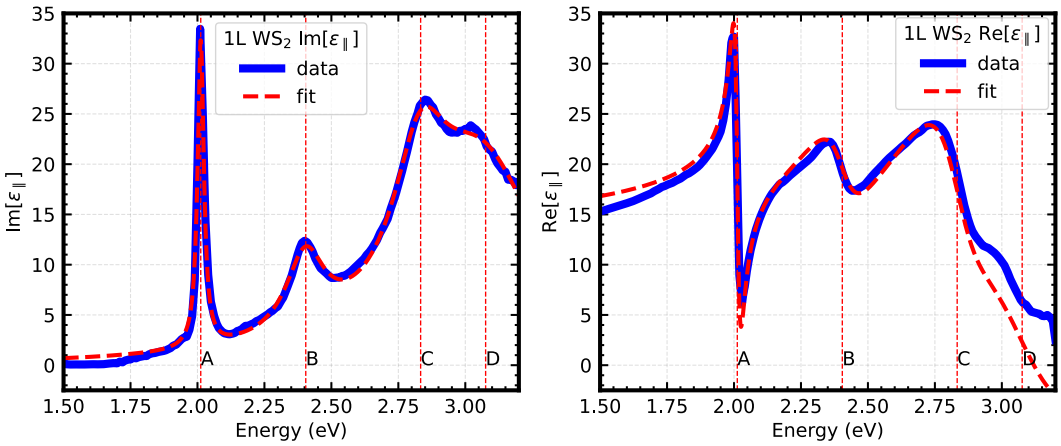

(a) (b)

Figure 2.2. Experimentally obtained data taken from [61] and fit of (a) the imaginary and (b) the real part of the dielectric function of 1L WS_2. Dashed vertical lines indicate the peak energy of the *A, B, C, D* features [10].

First, we fit the imaginary part of the experimentally derived dielectric function by combining four Lorentzian oscillators. Then, we determine the dielectric function's real part based on the imaginary part's fitting outcomes. We refine the computed real part by adjusting ϵ_b to ensure consistency with the experimentally observed $\epsilon_\parallel$. Finally, we derive the dielectric function of 1L WS_2 using Equation (2.5) and incorporating the fitting outcomes as shown in Figure 2.2.

We utilize the experimentally available data on the effect of strain on resonances of 1L WS_2. *A* exciton shifts by -45.2 meV/% strain, B exciton shifts by -35.7 meV/% strain, and C feature shifts by -20.7 meV/% strain in 1L WS_2 [43], [67, 68].

In our analysis, we disregard the alteration of the *D* characteristic since there's insufficient literature data. Given its significant distance from the emission range of QD and its minimal impact, it doesn't influence our computations. We also omit the effect of strain on oscillator strengths and linewidths, as they are insignificant for 1L WS_2. We also assume that the previously mentioned statements remain valid across the strain values reported in this study. So, to obtain the strain-dependent $\epsilon_\parallel$, we shift the exciton peak positions only, as shown in Figure 2.3.

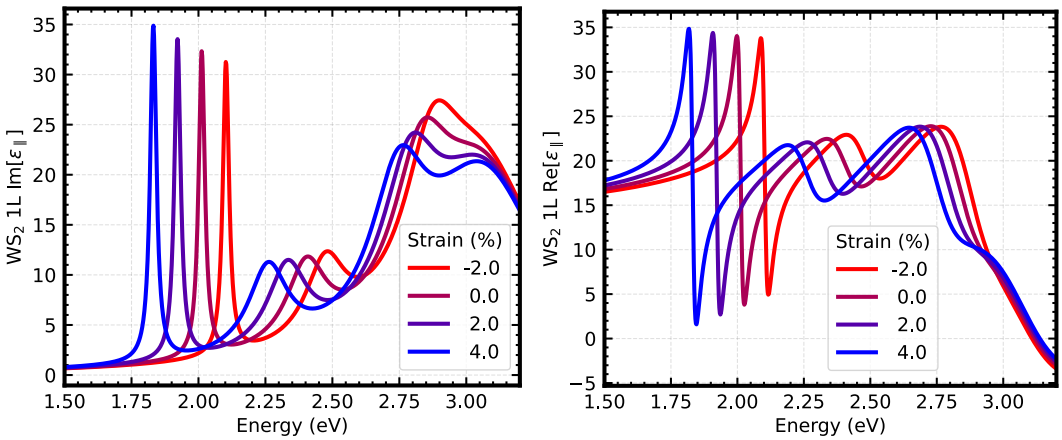

(a) (b)

Figure 2.3. Calculated strain-dependent complex dielectric functions of 1L WS_2: (a) imaginary part, (b) real part [10].

As for $\epsilon_\perp$, we use the experimentally available data [69] and take it as a constant ($\epsilon_\perp = 7$) in the interested energy range.

2.2.2. Determining PL Spectrum and Size of the ZnCdSe/ZnSe Core-Shell QD

In this section, the QDs are ZnCdSe/CdSe core-shell QDs from Sedat Nizamoğlu (Koc University).

Since QDs are typically clustered together instead of existing as individual particles, the uneven distribution within these clusters leads to PL spectrum characterized by a Gaussian lineshape $G(x)$ [70]

$$G(x) = A \times exp\left(-\frac{(x-\mu)^2}{2\sigma^2}\right), \tag{2.6}$$

where A is the amplitude (peak height) of the Gaussian curve, μ is the mean (center) of the Gaussian curve, σ is the standard deviation (width) of the Gaussian curve, and x is the independent variable. In our case, x represents frequency.

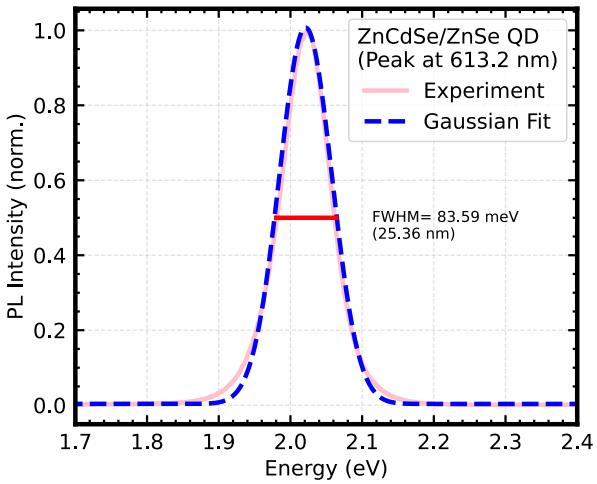

Figure 2.4. Gaussian fit to the PL spectrum of the QD.

Therefore, we analyze the PL of this ZnCdSe/ZnSe QD sample using a Gaussian fitting method, resulting in a peak observed at 613.2 nm, as shown in Figure 2.4.

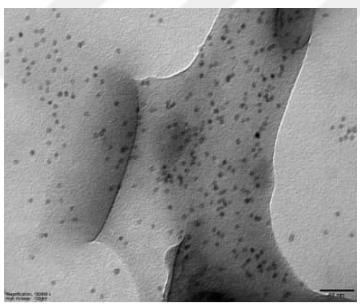

(a)

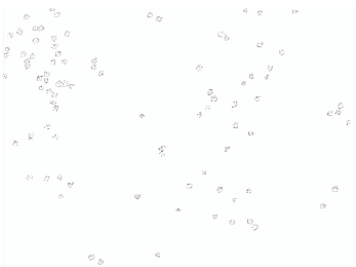

(b)

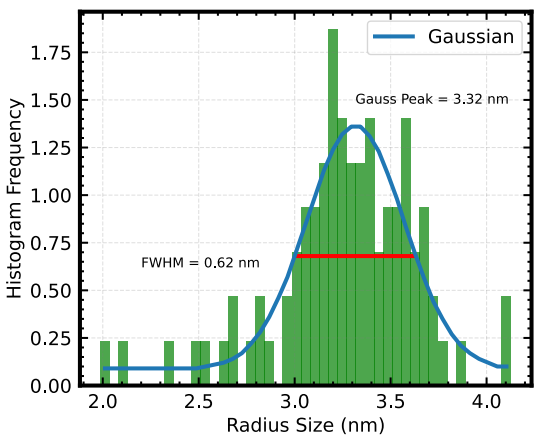

(c)

Figure 2.5. (a) The image of QD under TEM, (b) the outlines of the selected QDs, (c) the histogram created using the areas outlined in the TEM images.

We analyze the TEM images shown in Figure 2.5a to decide the radius. First, we apply a bandpass filter to the image and then manipulate the contrast and brightness

of the image to make QDs more detectable. Then, we set a color threshold to find the outlines of the QDs. Since, some places in the picture have a similar color frequency to the QD, we set area and circularity thresholds to eliminate unwanted areas. Only the areas lie between the range 10 - 100 nm^2, and objects with the circularity 0.60 - 1.00 remained. With these restrictions, we have an outline picture that we can work on, as shown in Figure 2.5b. The program that we use [71] gives us the area of these outlined objects. From the areas, we get the radii that produce these areas. We create a radius histogram with these values and make a Gaussian fit to this histogram. From this fit, we get the radius of the ZnCdSe/CdSe core-shell QD as 3.32 nm as presented in Figure 2.5c.

2.2.3. Total NRET as a Function of Strain

Following the aforementioned steps, we compute the strain-dependent NRET rate between the QD and the 1L WS_2. In calculations, we took d as the radius of the QD [72] and t as the thickness of 1L WS_2 (0.62 nm [53]). We would like to note that because QDs are spherical and much smaller than the wavelength of light, they can be considered as dipoles located at their center for spontaneous emission [73].

Figure 2.6 illustrates the NRET rate normalized by the dipole emission to vacuum $\Gamma_{\text{QD-2D}}/\Gamma_0$, plotted against energy for various strain levels. Due to the minimal thickness of the material, the screening effect, primarily governed by the real part of $\epsilon_{\parallel}$, does not dominate. Consequently, the NRET rates depicted in Figure 2.6a closely resemble the imaginary part of $\epsilon_{\parallel}$ of WS_2.

Figure 2.6b displays the product of the normalized PL of QDs and the NRET rate $\text{PL}_{QD} \times \frac{\Gamma_{\text{QD-1L WS}_2}}{\Gamma_0}$ under strain as a function of energy. This rate predominantly reflects the overlap between the A exciton peak in the $\text{Im}[\epsilon_{\parallel}]$ of 1L WS_2 and the PL_{QD} spectrum, which varies significantly with the applied strain.

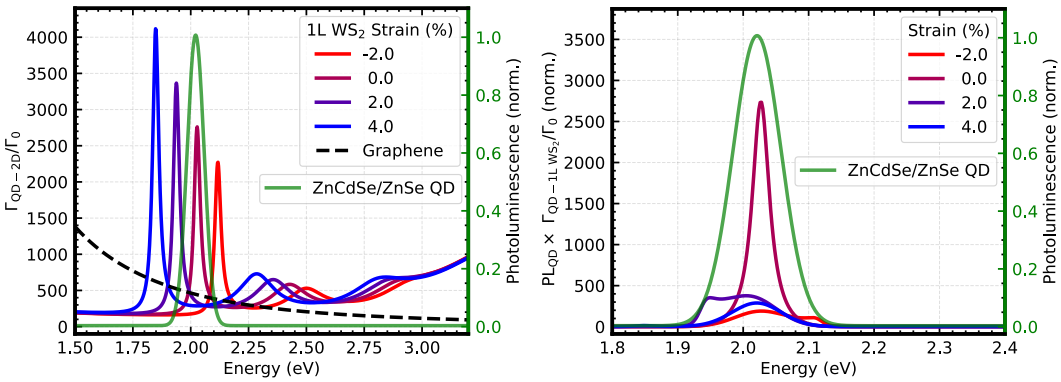

(a) (b)

Figure 2.6. (a) Calculated NRET rate (normalized by Γ_0) from QD to 1L WS_2 for selected strain levels (1L graphene for comparison), (b) product of the normalized PL of QDs and the strain-dependent NRET rate [10].

To calculate the NRET rate corresponding to this particular emission spectrum, we integrate the product of the PL spectrum and Γ/Γ_0, then normalize it by the total emission of the QD using

$$\text{Total (s)} = \frac{\int_{1.5\text{ eV}}^{3.2\text{ eV}} \Gamma/\Gamma_0(\text{s,E}) \times \text{PL}_{\text{QD}}(\text{E})\text{dE}}{\int_{1.5\text{ eV}}^{3.2\text{ eV}} \text{PL}_{\text{QD}}(\text{E})\text{dE}}. \tag{2.7}$$

Here, s represents strain, E denotes energy, and PL_{QD} indicates the PL emission of the QD. We plot this strain-dependent function and theoretically determine the strain-dependent Γ/Γ_0 rate between the QD and 1L WS_2. Figure 2.7 illustrates the total NRET rate between a ZnCdSe/ZnSe QD and 1L WS_2 as a function of uniaxial strain.

As Figure 2.7 shows, the NRET rate peaks near 0% strain, primarily due to the favorable overlap between the QD's emission spectrum and the absorption of the unstrained 1L WS_2 A exciton. As strain levels increase beyond 0%, the A exciton undergoes a significant redshift, leading to a substantial reduction in the NRET rate, reaching a minimum of around 4% strain. For strains exceeding 4%, the QD peak begins to overlap with the WS_2 B exciton, causing the NRET rate to increase again. The ratio between the maximum and minimum NRET rates is approximately 4 and achievable within a relatively small range of around 4% uniaxial strain.

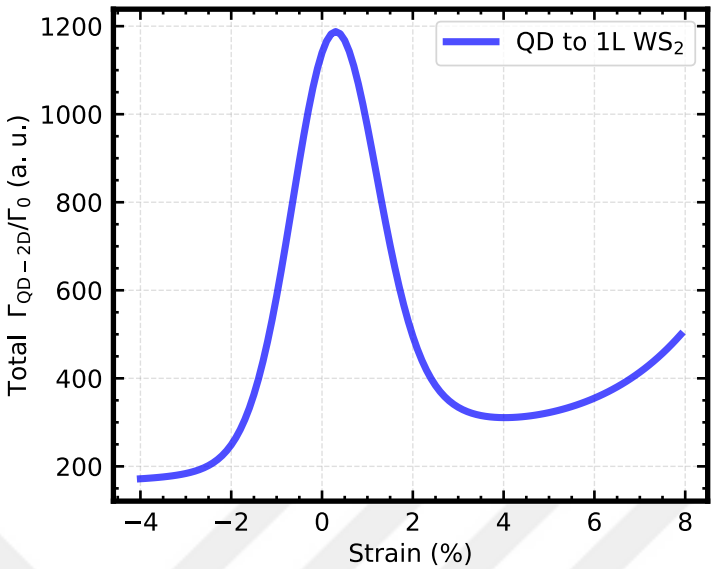

Figure 2.7. Total NRET rate between QD and 1L WS_2 as a function of strain [10].

2.3. Kramers–Kronig Constrained Variational Analysis of Optical Spectrum

The complex dielectric function $\epsilon(\omega) = \epsilon_1(\omega) + i\epsilon_2(\omega)$ has an impact on the linear macroscopic optical characteristics of materials. Generally, these quantities, $\epsilon_1(\omega)$ and $\epsilon_2(\omega)$ are studied by measuring them directly from the experiments. As an alternative, $\epsilon_1(\omega)$ and $\epsilon_2(\omega)$ can be extracted from each other since they are coupled with each other with Kramers-Kronig (KK) relations [74, 75]

$$\epsilon_1(\omega) - 1 = \frac{2}{\pi}\mathcal{P}\int_0^\infty \frac{x\epsilon_2(x)}{x^2 - \omega^2}dx, \tag{2.8}$$

$$\epsilon_2(\omega) = -\frac{2\omega}{\pi}\mathcal{P}\int_0^\infty \frac{\epsilon_1(x)}{x^2 - \omega^2}dx + \frac{4\pi\sigma_{DC}}{\omega}, \tag{2.9}$$

where $\mathcal{P}$ represents the priciple value integral and σ_{DC} is the direct-current conductivity.

The preceding arguments in this section follow the Kramers–Kronig constrained variational analysis utilized by Kuzmenko [76]. KK-constrained variational fitting is a multi-oscillator model where the number of Drude-Lorentz oscillators is within the

limit of the experimental points

$$\epsilon(\omega) = \epsilon_\infty + \sum_{k=1}^{N} \frac{\omega_{p,k}^2}{\omega_{0,k}^2 - \omega^2 - i\omega\gamma_k}, \tag{2.10}$$

with three adjustable parameters the plasma frequency $\omega_{p,k}$, the oscillator frequency $\omega_{0,k}$, the linewidth γ_k and the parameter ϵ_∞ corresponds to the contribution from higher-frequency oscillators. The oscillators that are not bound (representing conductivity electrons) are described using Drude terms, with $\omega_{0,k} = 0$ representing their characteristic frequency. With this approach, the analysis takes a model-independent form.

We would like to note that the Drude-Lorentz oscillator formula already satisfies the Equation (2.8) and Equation (2.9).

Generally, the number of oscillators, N, is very small compared to the experimental points; thus, the obtained spectrum, $\epsilon(\omega)$, is smooth, causing an information loss. Therefore, taking the N in the order of the experimental points can help to obtain the spectrum information independent from the model. But there is hindsight: the Drude-Lorentz oscillator has three parameters, and if all $3 \times N$ parameters are free to change, it is highly likely to result in an unstable model. So, we need to fix some parameters. We need a flexible fitting function to have spectral weight in the whole range, and this is achievable by placing an oscillator at every anchor frequency $\omega_{0,i} = \omega_i$. Additionally, the oscillators should be narrow so that they would only affect their neighbors. So, by fixing the frequencies and the linewidths in Equation (2.10), there is only one free parameter left: the oscillator strength.

Combining this method with the transfer matrix model, we can obtain the dielectric function, $\epsilon(\omega)$, from the experimentally obtained reflectivity spectra. For the thin films, the reflectivity of the film and substrate in the normal incidence is calculated

as [77]

$$R = \left| \frac{r_f + t^2 r_{fs}}{1 + t^2 r_f r_{fs}} \right|^2, \tag{2.11}$$

where

$$r_f = \frac{1 - \sqrt{\epsilon_f}}{1 + \sqrt{\epsilon_f}}, \quad r_{fs} = \frac{\sqrt{\epsilon_f} - \sqrt{\epsilon_s}}{\sqrt{\epsilon_f} + \sqrt{\epsilon_s}}, \quad t = \exp\left(i \frac{\omega}{c} \sqrt{\epsilon_f} d\right). \tag{2.12}$$

In the Equation (2.12), d is the thickness of the thin film, $\epsilon_f(\omega)$ and $\epsilon_s(\omega)$ represents the dielectric function of the film and the substrate, respectively.

The analysis consists of two steps: first, we make a fit to obtain reflectivity spectra (R) experimentally, and then from the fit, using Equation (2.11), we obtain the $\epsilon(\omega)$. For accurate analysis, we need data across the entire energy range. This is because the coupling properties of ϵ_1 and ϵ_2 require information at all energy levels, as described by Equations (2.8) and (2.9). But our setup covers the energy range between 1.6 eV $<$ E $<$ 3.1 eV. Fortunately, we can ignore the dielectric response at lower energies since polar phonons and free carriers dominate the response, which are weak [14], [78, 79]. For the high energy levels, we use the fact that the bulk dielectric function of TMDCs is similar in the few-layer limit and use the bulk data from the literature [80] as the dielectric response.

In our analysis, we placed an oscillator at every 2 meV within the range of 1.65 eV to 3.00 eV with a fixed linewidth of 2 meV.

We used this method to obtain $\epsilon(\omega)$ of the 1/2L WS_2 as shown in Figure 2.9 and 2-5L MoS_2 as shown in Figure 2.10 along with the $\epsilon(\omega)$ of the suspended 2L MoS_2 as shown in Figure 2.11.

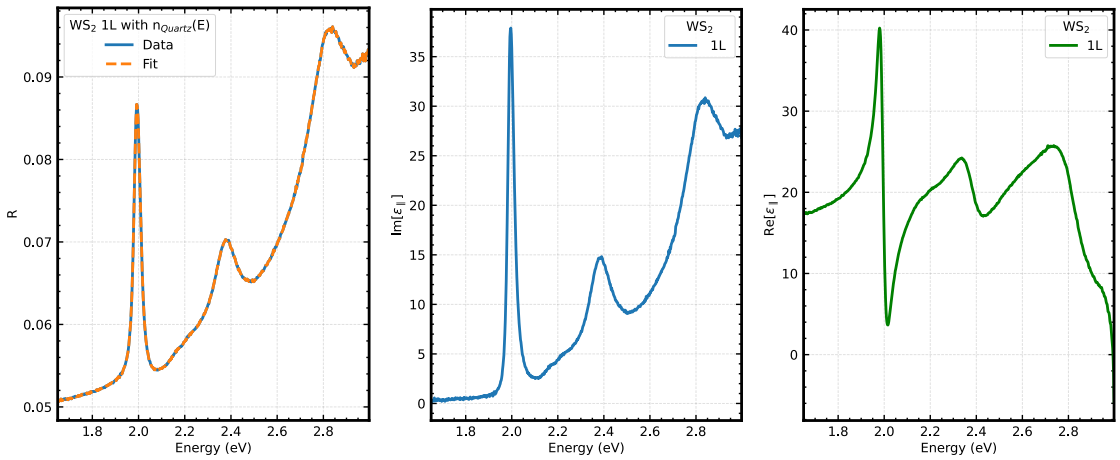

(a) (b) (c)

Figure 2.8. (a) Fitting Drude-Lorentz oscillators to Reflection Spectra of the 1L WS_2. (b) $Im[\epsilon_{\parallel}]$, (c) and $Re[\epsilon_{\parallel}]$ spectra of the 1L WS_2 obtained using KK-constrained variational analysis.

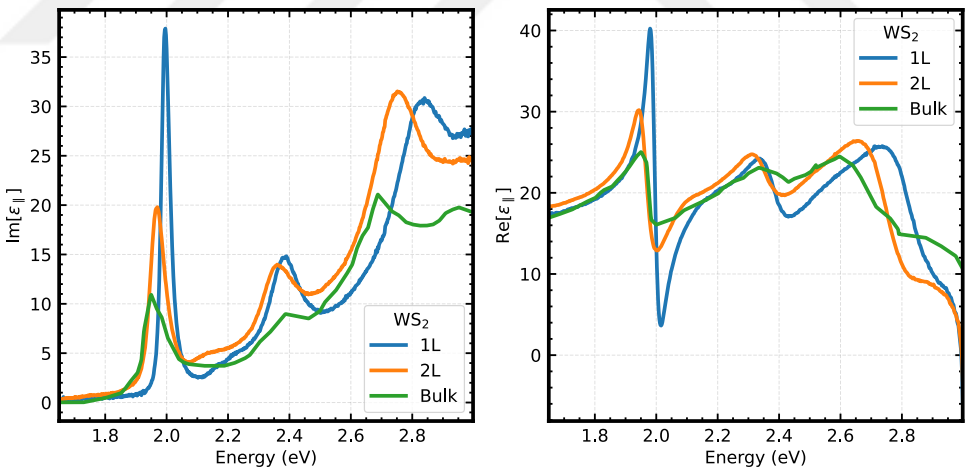

(a) (b)

Figure 2.9. (a) $Im[\epsilon_{\parallel}]$, (b) and $Re[\epsilon_{\parallel}]$ spectra of the 1L and 2L WS_2 obtained using KK-constrained variational analysis compared with bulk WS_2.

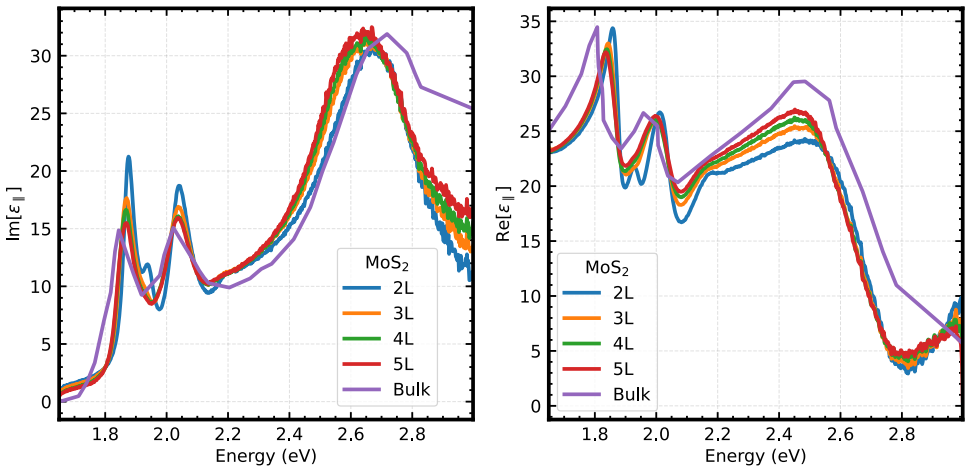

(a) (b)

Figure 2.10. (a) Im[$\epsilon_{\|}$], (b) and Re[$\epsilon_{\|}$] spectra of the 2-5L MoS_2 obtained using KK-constrained variational analysis compared with bulk MoS_2.

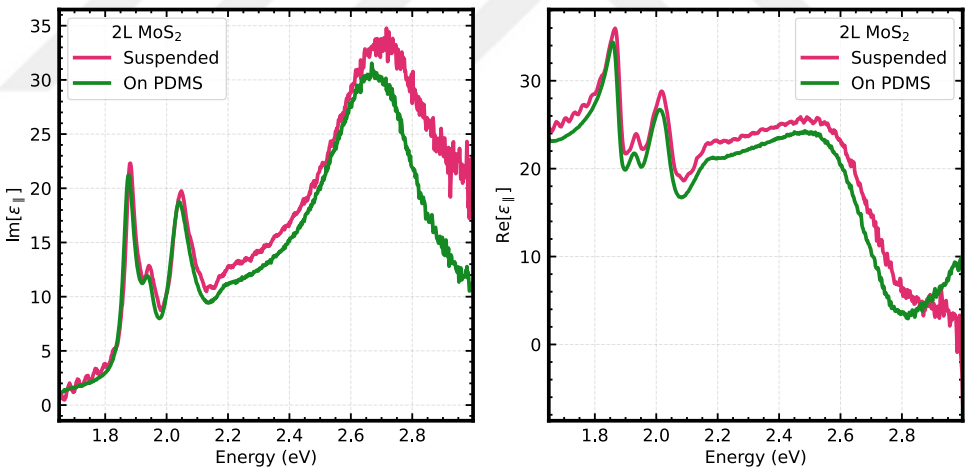

(a) (b)

Figure 2.11. (a) Im[$\epsilon_{\|}$], (b) and Re[$\epsilon_{\|}$] spectra of the suspended 2L MoS_2 obtained using KK-constrained variational analysis compared with the 2L MoS_2 on PDMS.

3. EXPERIMENTAL METHODS

This chapter explains the experimental techniques and the methods we use to analyze the data obtained from our research.

3.1. Mechanical Exfoliation

Mechanical exfoliation is a technique to obtain a few-layer TDMC from bulk crystal using tape. Since the VdW bond is weak within the layers, using external mechanical force is enough to overcome the force.

We use band-assisted exfoliation as our exfoliation technique. We perform the mechanical exfoliation at the Advanced Functional Materials and Devices Research Laboratory at Istanbul University (Laboratory of Assos. Prof Fahrettin Sarcan). The procedure begins by pressing wafer tape onto bulk WS_2. Next, we cut a piece of PDMS to approximately 1 cm x 1 cm and place it on a slide. We then carefully lift the wafer tape from the bulk WS_2 and gently press it onto the surface of the PDMS. After waiting for about 1-2 minutes, we gently lift the wafer tape, completing the exfoliation process. With this technique, the forces acting on the bulk crystal can be separated as normal force $F_{\parallel}$ and the lateral force $F_{\perp}$ as shown in Figure 3.1. $F_{\perp}$ helps to break the VdW and separates the layer and $F_{\parallel}$ the layer laterally [81].

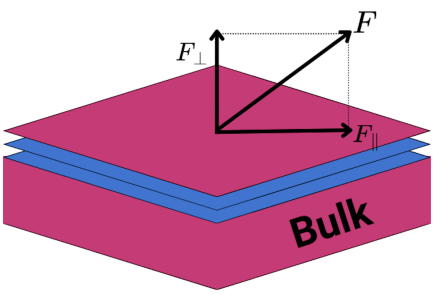

Figure 3.1. Diagram showing the forces on the bulk crystal during exfoliation.

After exfoliation, we scan the surface of PDMS with an optical microscope and choose possible candidates for the desired number of layers WS_2.

3.1.1. Notes on Exfoliation

When the waiting time is around one minute, we find 2L with the same reoccurrence rate as 1L. When we increase the waiting time to around four minutes, we cannot find as much 2L WS_2 compared to one minute, and we mostly come across 1L. However, the 2Ls we found are more considerable than the shorter waiting time. After the waiting time exceeds six minutes, we come across mostly with 1L and almost find no 2L.

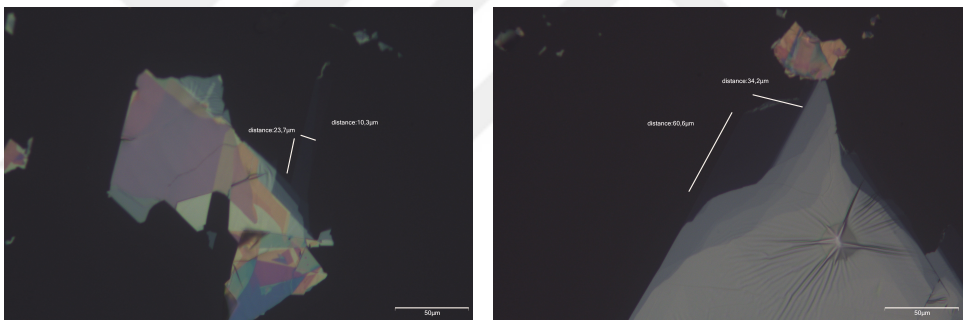

(a) (b)

Figure 3.2. Result of difference between waiting time around: (a) one minute, (b) four minutes.

3.2. Optical Measurements

We rely on optical measurements to understand and investigate the properties of thin films. For example, PL measurements are crucial for studying thin films, providing information about exciton dynamics and carrier recombination, whereas reflectance measurements help characterize material properties like position, refractive index, and absorption by analyzing how light reflects off the surface. TRPL is critical for understanding carrier recombination and exciton behavior, offering insights into excited state lifetimes and distinguishing between radiative and nonradiative processes. PL map-

ping allows us to map optical properties across a surface, identifying inhomogeneities, defects, and strain distributions

3.2.1. Setup

We perform the reflectance and PL measurements in our custom-built setup as illustrated in Figure 3.3. The path for the laser we use for PL follows the green line, and the path for reflectance follows the white line. We switch between reflectance and PL measurement by changing the position of the mirror before the blue line shown in Figure 3.3.

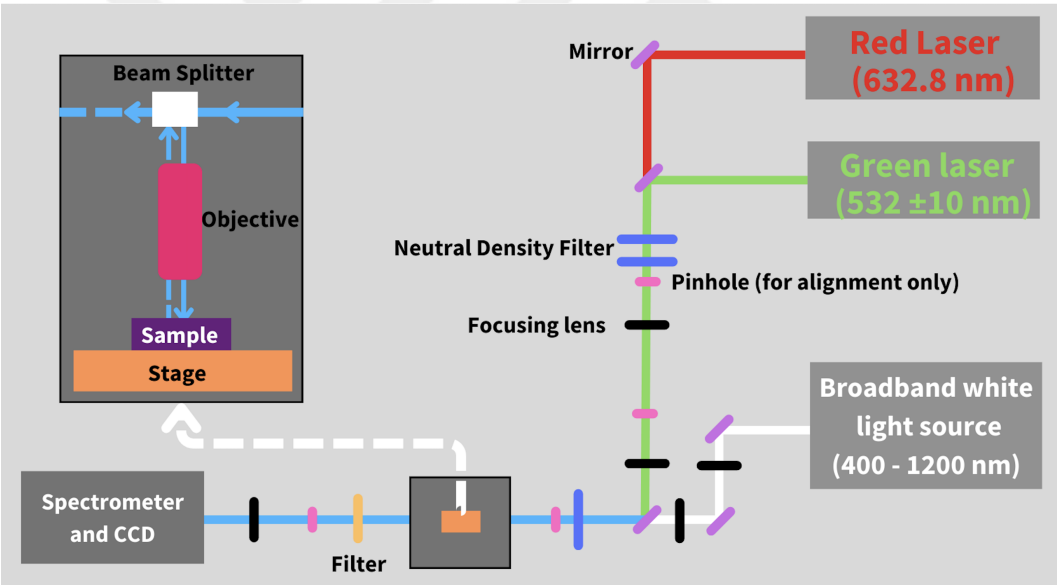

Figure 3.3. Diagram of the optical setup, same colored elements represent the same items.

The TRPL measurements take place at Bilkent University UNAM center (Laboratory of Dr. İbrahim Sarpkaya) and PL mapping at the same laboratory as the exfoliation.

3.2.2. Measurement Process

We calibrate our setup using the red laser that emits photons with a wavelength of 632.8 nm. To perform measurement experiments, we first open the Monochromator application from the computer and open the slits, and set the calibrated wavelength to 632.8 nm. Then, we open Andor software and set the temperature to -50°C. We focus on the sample by moving the stage to the z-axis and find it by using x-y directions.

For the PL measurements, we follow the steps:

(i) Place a 550 nm long-pass filter before the CCD.
(ii) In Andor Sofware, set the acquisition mode to single.
(iii) Set the acquisition time.
(iv) Open the green laser and increase the current to 1.90 - 2.10 A.

For the reflectance measurements, we follow the steps:

(i) Place a 420 nm long-pass filter before the CCD.
(ii) In Andor Sofware, set the acquisition mode to accumulate.
(iii) Set the acquisition time.
(iv) Open the white light source and increase the power to the middle.

Lastly, we get the measurements and analyze the data.

3.2.3. Analysis of the Measurements

3.2.3.1. PL Measurement Analysis. For the analysis of the PL data, first, we subtract the substrate data from the sample data and we interpolate the substracted data with a desired array as illustrated in Figure 3.4.

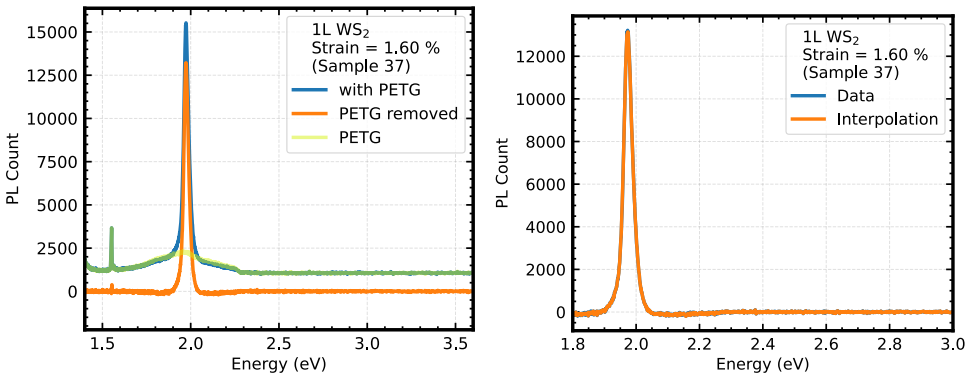

(a) (b)

Figure 3.4. (a) Subtraction of the substrate data (PETG) from the sample data, (b) interpolation of the substracted data with a given array.

Then, to eliminate the unwanted noise, we remove the outlier spikes from the interpolated data, as shown in Figure 3.5.

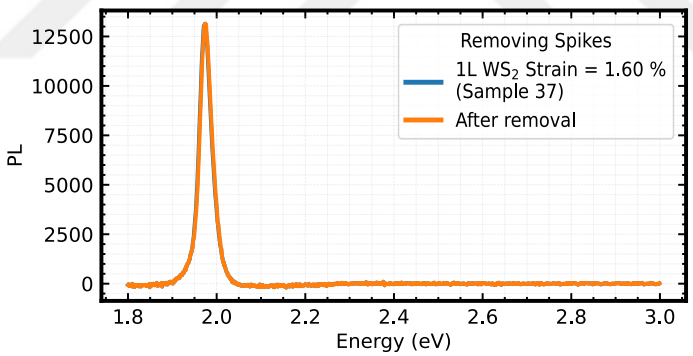

Figure 3.5. Removing spikes from the interpolated data.

We set a new baseline for the data as shown in Figure 3.6. Then, to get the true representation of the data, we perform efficiency corrections to the data and analyze the obtained peak as shown in Figure 3.7.

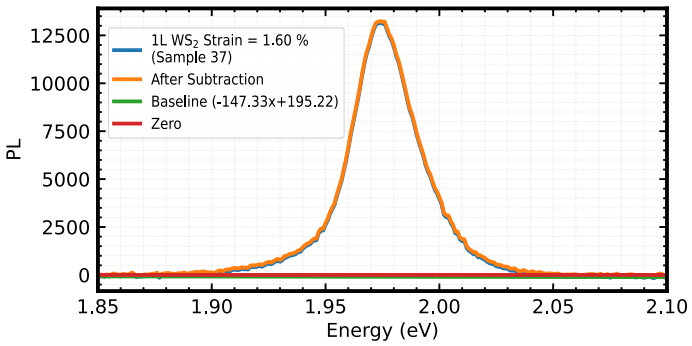

Figure 3.6. Setting a new baseline for the data.

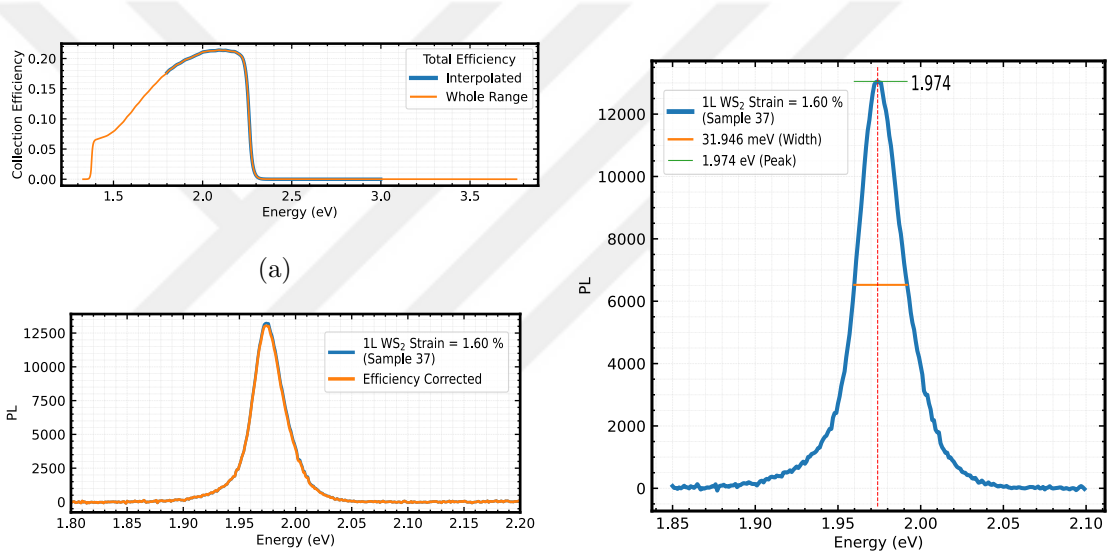

Figure 3.7. (a) Collection efficiency of the setup, (b) efficiency corrected data, (c) peak analysis of the data.

3.2.3.2. Reflectance Measurement Analysis. To analyze the data from the reflectance measurement, we first need to change the data format and obtain the reflection contrast since the count we obtain from the sample is the combined count from the sample, the substrate, and the background as illustrated in Figure 3.8. We calculate the reflection contrast $\Delta R/R_{\text{Substrate}}$ using

$$\frac{\Delta R}{R_{\text{Substrate}}} = \frac{R_{\text{Sample}} - R_{\text{Substrate}}}{R_{\text{Substrate}} - R_{\text{BG}}}, \tag{3.1}$$

where R_{Sample} represent the reflectance of the thin sample on the substrate (or no substrate), $R_{\text{Substrate}}$ is the reflectance of the substrate, and the R_{BG} is the reflectance without any sample or substrate as represented in Figure 3.8.

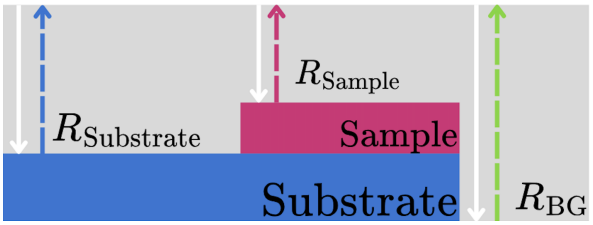

Figure 3.8. Schematic of the reflectance measurement.

Figure 3.9b illustrates the $\Delta R/R_{\text{PDMS}}$ obtained using the reflectance measurements shown in Figure 3.9a.

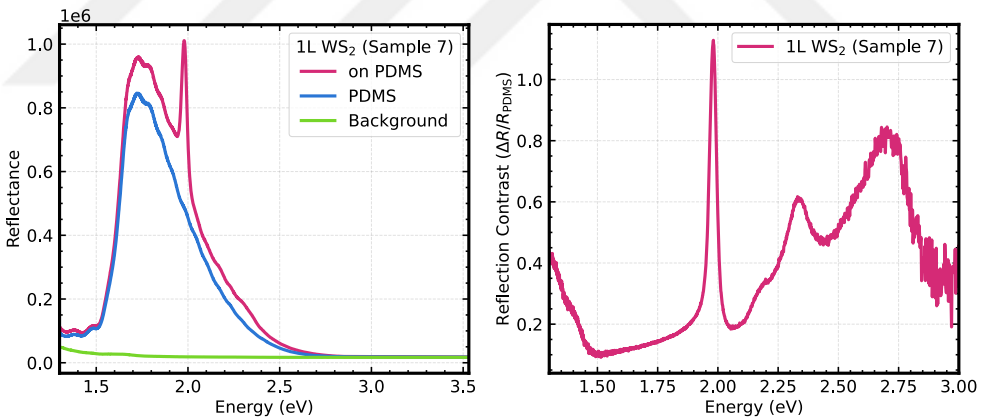

(a) (b)

Figure 3.9. (a) The reflectance measurements from 1L WS_2, PDMS and the background, (b) reflection contrast spectrum of 1L WS_2 on PDMS substrate.

To get the reflection of the material R, we also need the reflection of the substrate R_{Subs}. We calculate it by

$$R_{\text{Subs}} = \left| \frac{n_{\text{Subs}} - 1}{n_{\text{Subs}} + 1} \right|^2, \tag{3.2}$$

where n_{Subs} is the refractive index of the substrate. Figure 3.10b shows the R_{PDMS}

calculated from n_{PDMS} shown in Figure 3.10 using Equation (3.2).

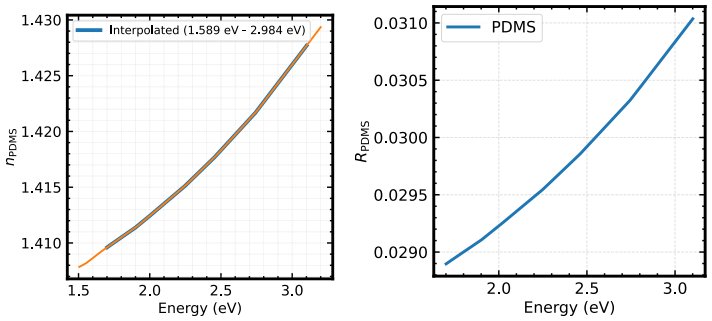

(a) (b)

Figure 3.10. (a) Refractive index of PDMS n_{PDMS}, (b) reflection from PDMS R_{PDMS}.

When we have the R_{Subs}, we can compute R by

$$R = R_{\text{Subs}} \times \left(1 + \frac{\Delta R}{R_{\text{Subs}}}\right). \tag{3.3}$$

Analyzing the reflectance spectra gives us information about the excitons' positions, linewidths, and strengths. Thus, we model the reflectance spectra as a superposition of 7 Lorentz oscillators, each oscillator corresponding to A_{1s}, A_{2s}, A_{3s}, B_{1s}, B_{2s}, C, and D excitons respectively as shown in Figure 3.11.

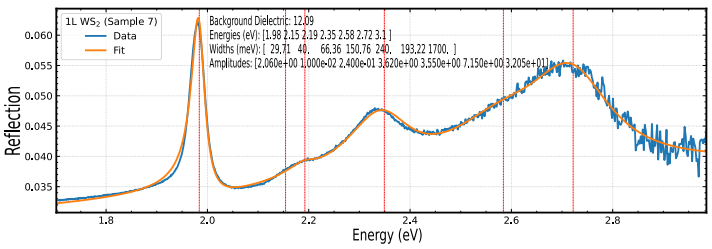

Figure 3.11. Result of the fitting Lorentz oscillators to the exciton positions of the $R_{\text{1L WS}_2}$.

3.2.3.3. TRPL Measurement Analysis. To analyze the TRPL data, we must first deconvolute using the instrument response function (IRF). Deconvoluting TRPL data using IRF is essential for accurate and reliable measurements. It accounts for the

detection system time and ensures the decay profiles represent the sample dynamics. Deconvolution also removes systematic effects, facilitates comparison across different experiments, and provides a correct baseline for quantitative analysis. Additionally, it improves the signal-to-noise ratio by correcting for variations in detection efficiency. As our deconvolution method, we choose the Wiener Deconvolution Method. The noise power in the analysis depends on the data and the system.

To perform deconvolution, we must normalize our data first. We rescale the "Count" values to a range between zero and one, where zero corresponds to the minimum value, and one corresponds to the maximum value using

$$\text{Normalized Value} = \frac{\text{Original Value - Minimum Value}}{\text{Maximum Value} - \text{Minimum Value}}. \tag{3.4}$$

After normalizing, we can deconvolute as shown in Figure 3.12b.

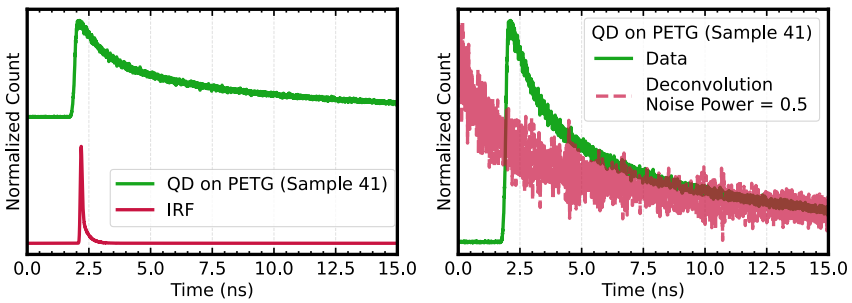

(a) (b)

Figure 3.12. (a) Normalized data and IRF obtained from TRPL measurements, (b) deconvoluted data obtained from deconvolution of the TRPL data.

The excitons experience an exponential decay

$$\text{Decay} = A \times e^{-(x-x_0)\lambda} + C, \tag{3.5}$$

where A represents the amplitude of the decay, x is the independent variable (in our case, time), x_0 is the reference point along the x-axis, λ is the decay constant indicating

the rate of decay, and C is the offset or baseline value that the decay approaches. So, we make an exponential fit to the deconvoluted data using Equation (3.5) and obtain the decay constant λ as shown in Figure 3.13. From the constant λ, we can get the lifetime of the excitons by $\tau = 1/\lambda$.

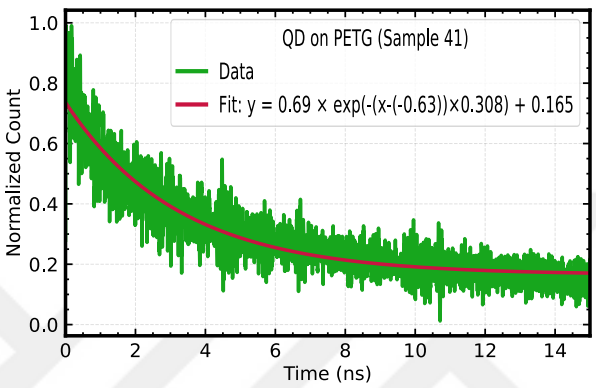

Figure 3.13. Result of the fitting exponential decay to the deconvoluted data.

3.3. Dry Transfer of 2D Materials

We used the transfer system at the Advanced Functional Materials and Devices Research Laboratory at Istanbul University (Laboratory of Assos. Prof Fahrettin Sarcan), as shown in Figure 3.14.

The steps of the transfer are as follows :

(i) Locate the desired sample using an optical microscope in x5 magnification.

(ii) Using a pen, mark the image's corners under the microscope and obtain a small square with the sample in the center by cutting.

(iii) Place a PDMS on a slide and put the little cut square on top of the PDMS.

(iv) Adjust the setup temperature to a desired degree and place the substrate on the setup.

(v) Get the prepared slide and secure it to the setup.

(vi) Locate the desired sample for transfer and the place to transfer.

(vii) By following through the screen, carefully lower the slide onto the substrate as

shown in Figure 3.14b.

(viii) After ensuring the sample is stuck to the substrate, carefully raise the slide by following through the screen.

In such cases where transfer requires more precision, like transferring onto a hole, the help of the piezo stage is beneficial. By lowering and raising the voltage in the z-direction, the piezo stage makes the transfer process less prone to human errors.

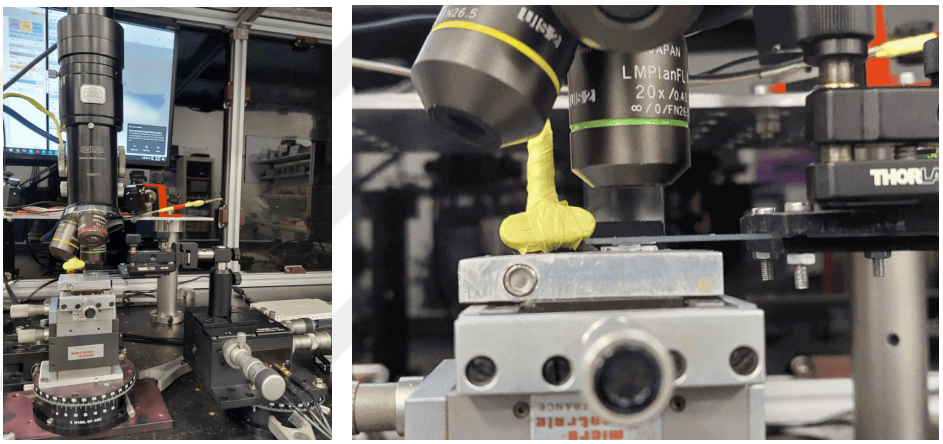

(a) (b)

Figure 3.14. (a) Transfer setup, (b) close-up to the transfer setup.

3.4. Strain Stage

To apply the strain, we use the three-point bending method. We can apply uniaxial strain to the material by placing the substrate in between the clamps, then by pushing the PETG substrate up from its mid-point, as shown in Figure 3.15a.

When placing the material, we consider its location so that it is close enough to the bending point for the strain transfer but far enough to eliminate light interaction with the metal. Then, we adjust the stage to ensure the material will be on 0% strain position.

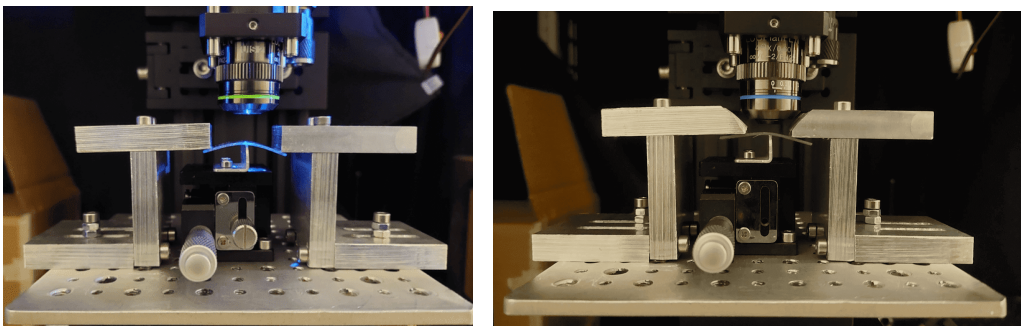

(a) (b)

Figure 3.15. Three-point bending strain apparatus: (a) initial design, (b) current state after filing to allow more space on top.

From geometry, the applied strain is determined by [82]

$$\text{Strain}(\%) = \frac{600 \times \text{Thickness}_{Subs} \times \Delta z}{(\text{Clamp Width})^2}, \tag{3.6}$$

where Thickness_{Subs} is the thickness of the substrate (in our case PETG), Δz is $\Delta z = |z_{\text{initial}} - z_{\text{final}}|$ where z_{initial} is the 0% strain position, and the clamp width is the distance between two clamp positions. Figure 3.16 gives more insight into the geometry of the strain.

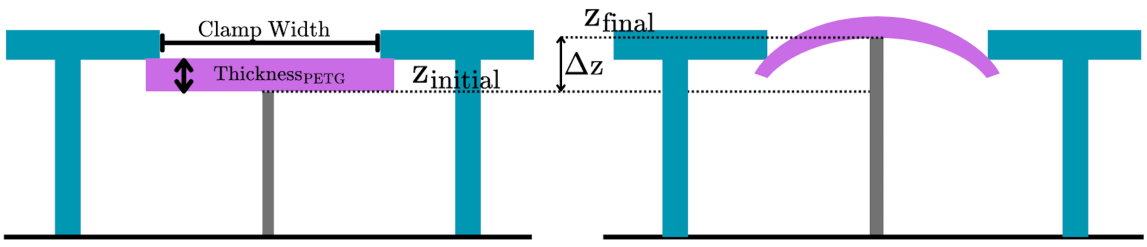

Figure 3.16. Schematic of the three-point bending apparatus and the flexible PETG substrate.

As Equation (3.6) states, the applied strain inversely correlates with the clamp width by its square. So, it makes sense to keep the clamp width short, but the objective we use has a short focal length. This requires PETG to be close to the objective, but we cannot easily move our stage when PETG is near. Thus, we filed the edges near the objective of more mobility, as illustrated in Figure 3.15b.

4. SUSPENDED WS_2

Working with suspended TMDC instead on a substrate offers distinct advantages, particularly in studying their intrinsic properties. The substrate often affects the TMDCs and can alter their electronic band structure, introduce strain, and affect charge carrier mobility, complicating the analysis of their fundamental behavior. In contrast, suspended TMDCs are free from these substrate-induced perturbations, allowing for a more precise investigation of their natural properties [83]. Additionally, suspended TMDCs often exhibit enhanced optical properties, such as increased PL intensity [84] since the absence of a substrate reduces photon quenching and scattering. This configuration also facilitates more precise strain engineering, as applying mechanical strain to a suspended TMDC can be more uniform and controlled, leading to more predictable changes in its electronic and optical characteristics [85].

This chapter focuses on our attempts to suspend 2L WS_2 and the challenges during this process. Unlike the theory, we prefer to work with 2L since the PL from 1L WS_2 is high, and we will not be able to distinguish it from the PL coming from QD.

4.1. Samples on Holes

As a substrate, we use quartz, and the holes are etched onto the quartz using a focused ion beam at the Nano & Optoelectronics Research Laboratory at Istanbul University (Laboratory of Assos. Prof Fahrettin Sarcan and Prof. Ayşe Erol). The first transfer we perform is onto a hole with a diameter of 6.5 μm and a depth of 20 μm. During the transfer, 2L WS_2 experiences a tear, making the transfer unsuccessful, as shown in Figure 4.1a. However, the tear does not hinder the optical measurement. As Figure 4.1b, PL coming from suspended WS_2 is almost quintuples the PL from WS_2 on a quartz substrate. But, when we perform the reflection measurement, we observe an interference pattern caused by light reflecting from the bottom of the hole as shown in Figure 4.1c.

To get rid of the interference, we decided to create deeper holes. We start to etch with a diameter of 6 μm. We have two sets of holes, with 30 μm and 40 μm deep. However, since the holes are deep, starting with 6 μm results in the holes being wider than we anticipate with a diameter of 8-9 μm. Larger holes cause multiple 2L WS_2's to tear during transfer, as presented in Figure 4.2b and c.

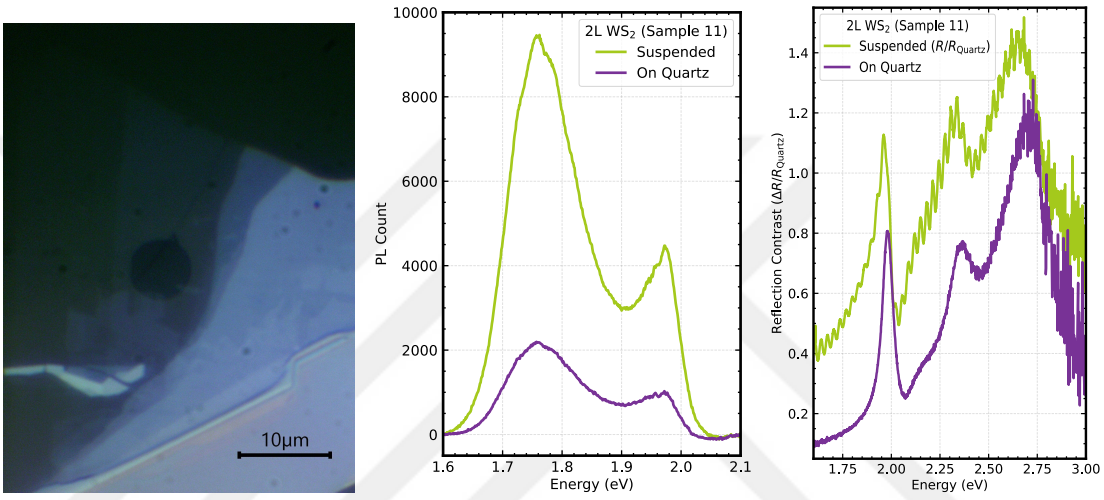

(a) (b) (c)

Figure 4.1. (a) Transfer of 2L WS_2 onto quartz substrate with hole, (b) PL spectra, (c) and $\Delta R/R_{\text{Quartz}}$ of 2L WS_2 on quartz substrate with hole.

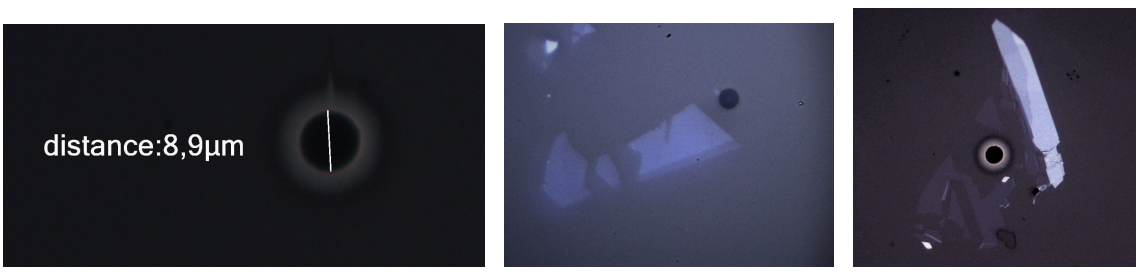

(a) (b) (c)

Figure 4.2. (a) Diameter of the hole etched on the quartz substrate. Tear during the transfer of 2L WS_2 onto a hole: (b) Sample 15, (c) Sample 24.

4.2. Spin-Coating of QD

In this section, the QDs mentioned are obtained from Koc University.

One of the crucial steps for our experiments is to place the QD onto WS_2. Normally, this is done by spin-coating the QDs onto the suspended WS_2. However, since our method of applying strain to suspended material is by air pressure, we want to refrain from any process that can harm the integrity of WS_2 on the hole, and spin-coating can result in tearing. Therefore, we came up with two alternative ideas that we could do instead of spin-coating. First, spin-coat the QD onto a glass slide, and then, in the transfer stage, the QD is transferred from the glass to the surface of WS_2 on PDMS. The second one is to spin-coat the surface of WS_2 on PDMS and then transfer it onto the membrane. First, we look into the literature [86–88] to determine the spin-coating parameters for spin-coating QD. After investigating, we decided to try the range 1100-2200 rotation per minute (rpm) with a duration ranging from 30 to 60 seconds. The spin-coating experiments done in the laboratory of Prof. Amitav Sanyal at Bogazici University.

4.2.1. Spin-Coating of Glass

We cut a glass slide into a square with a 1 cm x 1 cm dimension and spin-coat its surface. After trying several parameters, we decided that 1500 rpm with a duration of 60 seconds is the optimal parameter for us. In this parameter, we can scatter the QD somewhat evenly across, and PL is observed as depicted in Figure 4.3b. Plus, the time is enough for the toluene (dilution liquid for the QD) to dry.

We tried to transfer the QD onto WS_2 on PDMS. To increase the stickiness of the PDMS, we performed the transfer at 25 ^{o}C. After the transfer, we do not observe QD or their PL on the WS_2.

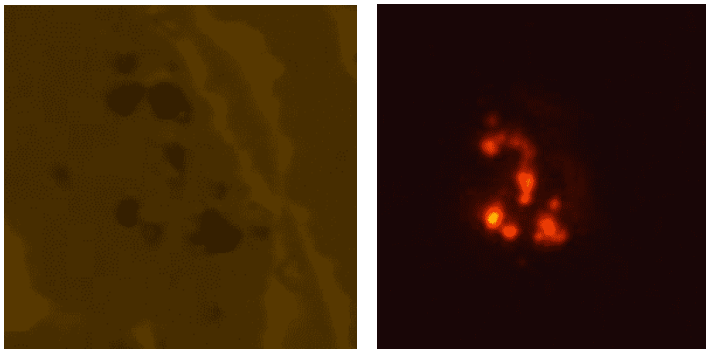

(a) (b)

Figure 4.3. (a) Spin-coating the QD onto a glass substrate, (b) PL from QD that is spin-coated onto the glass.

4.2.2. Spin-Coating of WS_2 Before Transfer (on PDMS)

We decided to use the same parameters we used for the glass (1500 rpm, 60s). We spin-coat the surface of an exfoliated WS_2 on PDMS. After the spin-coating, we cannot find the previously known WS_2 flakes as Figure 4.4 illustrates. When we look at the literature, we find that the surface of the PDMS swells with non-polar solvents such as toluene [89]. With this new information, we use ethanol-solved (polar solvent) QD to spin with the same parameters. There is no observable effect on the surface of the PDMS as Figure 4.5 illustrates, and PL from WS_2 is comparable to the before spin.

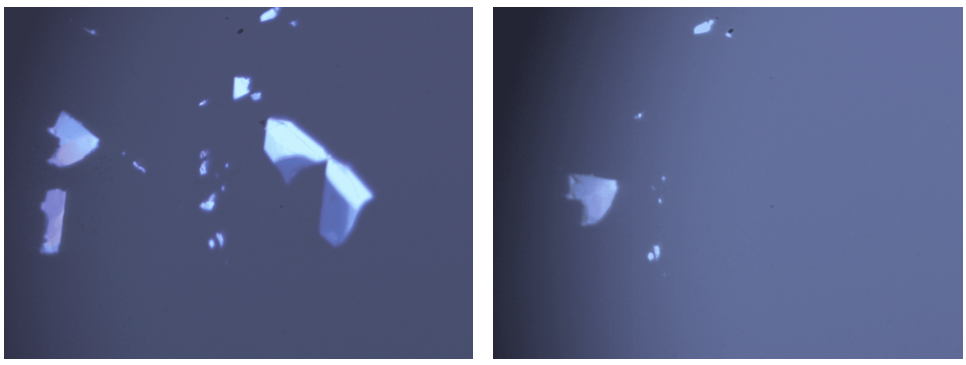

(a) (b)

Figure 4.4. The surface of PDMS (a) before, (b) after spin-coating with toluene.



(a) (b)

Figure 4.5. The surface of PDMS (a) before, (b) after spin-coating with ethanol.

5. SUPPORTED WS_2

We attempted to suspend 2L WS_2 several times but were unsuccessful due to tearing during the transfer process. Samples obtained through mechanical exfoliation are typically smaller, and 2L material often has cracks, and our etched holes have diameters of around 8 μm, and it is difficult to find large, defect-free samples. Consequently, our transfer attempts did not yield samples on holes capable of withstanding air pressure. We decided to use a three-point bending technique to apply strain to 2D materials on a flexible substrate, specifically Polyethylene Terephthalate Glycol (PETG) [41–43].

In this chapter, we explain how we applied strain to WS_2 and the effects of that strain.

5.1. Tranfer of WS_2 to PETG Substrate

We have three PETG sheets with different thicknesses and properties. We need to investigate their properties to decide what sheet to proceed with. First, we cut the Sheet 1 with 25 mm x 40 mm dimensions. We clean the surface with air, then try to transfer WS_2 as described in Section 3.3. However, as we raise the WS_2 after contact with the PETG surface, there is no transfer of WS_2 to PETG. So, we put the PETG on ozone treatment for four minutes to activate the surface. After the activation, the transfer is successful.

Since we do not want to change the surface of the PETG, ozone treatment is not applicable. Thus, we opt for a different PETG sheet, Sheet 2. We cut it with dimensions of 25 mm x 40 mm. To ensure the surface is clean, before the transfer, we put the PETG in distilled water, then place it into an ultrasonic cleaner for 15 minutes at 25°C and then dry it with air. When WS_2 and PETG are on top of each other, we wait around four minutes to help the transfer. The transfer is successful, as shown in Figure 5.1.

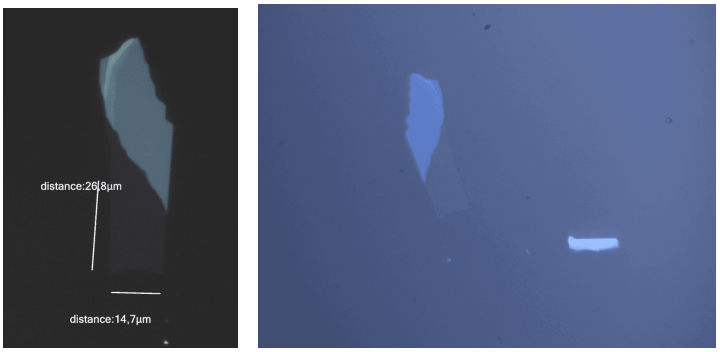

(a) (b)

Figure 5.1. Sample 33 on: (a) PDMS, (b) PETG after transfer.

Lastly, we make a transfer directly after removing the protective film from the surface of Sheet 2 with the dimensions 25 mm x 25 mm. Again, we waited for around four minutes. The transfer is successful, as shown in Figure 5.2.

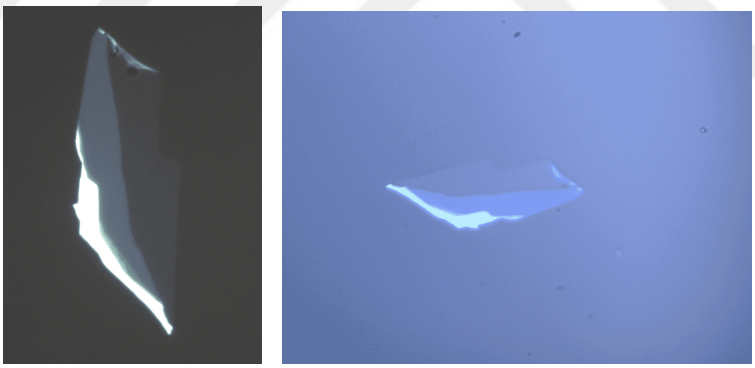

(a) (b)

Figure 5.2. Sample 37 on: (a) PDMS, (b) PETG after transfer.

From our three different PETG sheets, the surface of Sheet 1 is not sticky enough for WS_2 to transfer. We are only able to transfer when the surface is treated with ozone. Additionally, when the strain is applied to the transferred WS_2 on Sheet 1, we cannot observe the effect of the applied strain. The surface of Sheet 2 is sticky enough to transfer WS_2 without an extra process, and we can see the effect of the strain on this sheet. As for Sheet 3, it broke when we cut it with scissors. So, we proceed with Sheet 2 as our substrate.

Table 5.1. Investigated properties of the PETG sheets.

Sheet Number	Thickness (mm)	Transferable	Can we apply strain
1	1.0	No	No
2	0.8	Yes	Yes
3	1.0	No Data	No

5.2. Applying Strain to WS_2

We apply strain to PETG with Sample 33, with a clamp width of 37 mm, starting from 9.20 mm to 7.00 mm with decrements of 0.2 mm. Since the clamp width is long, the maximum applied strain is 0.77% according to the Equation (3.6). We perform PL measurements to three points within the same strain level since strain may not transfer at every point. We confirm this by looking at the PL spectra as shown in Figure 5.3, where the same colored lines represent the same strain levels. We have different peak positions, linewidth, and amplitudes for the same level of strain. While taking data, we observed that the points away from the bulk showed more drastic changes in their spectra.

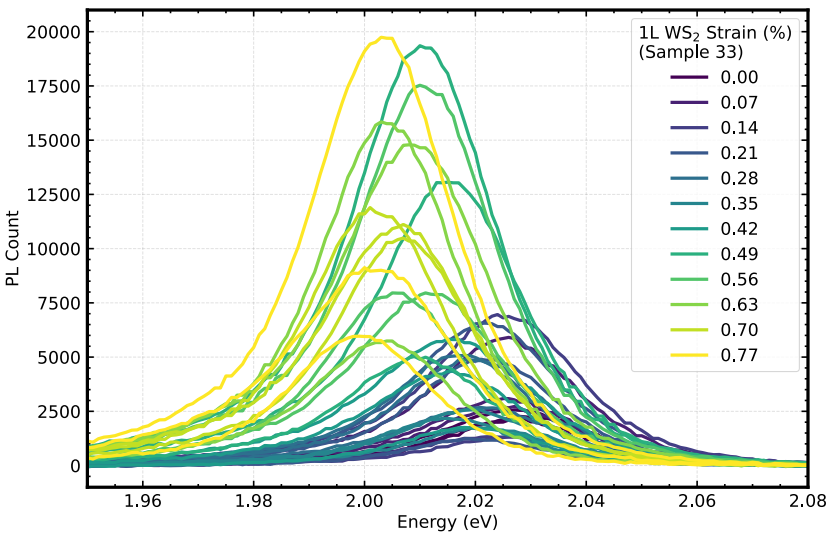

Figure 5.3. PL spectra of Sample 33 with the clamp width of 37 mm, same colored spectra represent the same strain level.

When we further analyze the PL spectra, we observe no correlation between linewidth and strain as shown in Figure 5.4a, but there is a consistent change in the peak position as a function of strain, as Figure 5.4b shows.

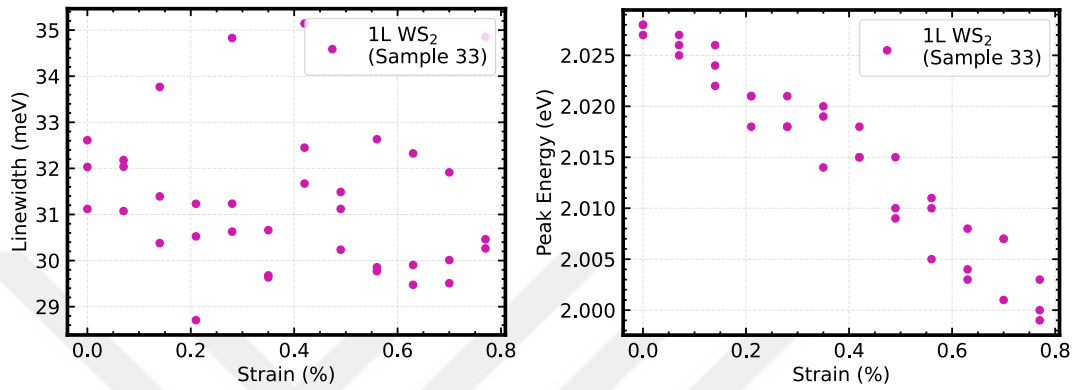

(a) (b)

Figure 5.4. Strain-dependent (a) linewidth, (b) peak energy analysis of the PL spectra of Sample 33 with the clamp width of 37 mm.

We conclude that the strain levels we apply are too small to comment on any relation, and the maximum strain that we applied (0.77 %) is reversible for 1L WS_2. So, we turn the PETG and make our clamp width narrower (18 mm) to apply more strain with the same decrements. We start from 9.00 mm and end at 7.00 mm with 0.2 mm decrements. We take data from 3 locations at the same strain level and again observe different spectra for the same strain level as illustrated in Figure 5.5a. The observation of locations further away from the bulk transferring the strain better continued in this orientation as well.

This time, when we analyze the relation between strain and the spectral features, we can see the effect of the strain as shown in Figure 5.5a and b. There is a redshift in the peak position, and the linewidth decreases with the increase in the strain.

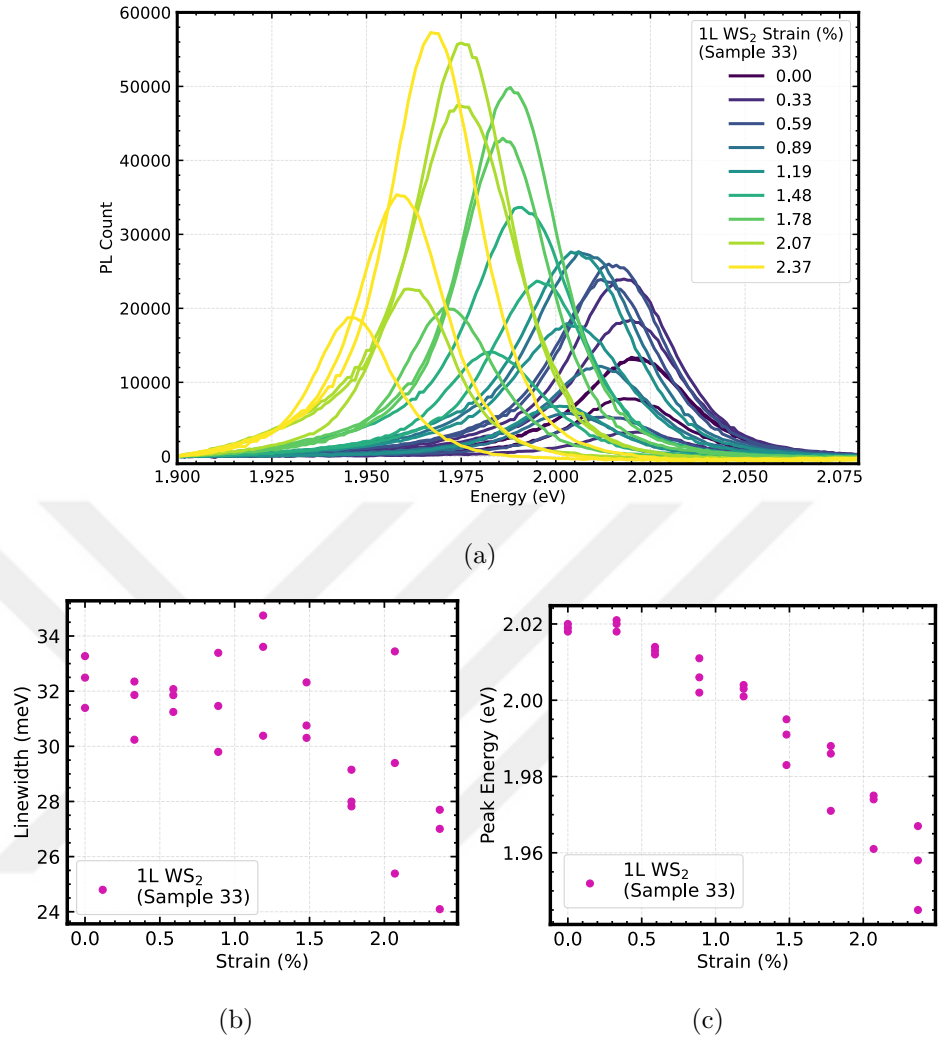

(a)

(b) (c)

Figure 5.5. (a) PL spectra, (b) strain-dependent linewidth, (c) and peak energy analysis of the PL spectra of Sample 33 when the strain was applied the second time with the clamp width of 18 mm.

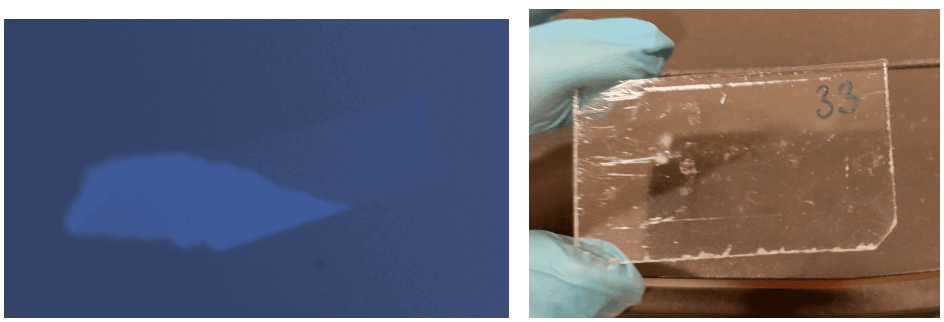

(a) (b)

Figure 5.6. (a) Sample 33 after the strain applied, (b) PETG substrate after strain is applied.

At the 2.37% strain limit, we observe structural damage on the WS_2 as shown in Figure 5.6a. There are cracks throughout the sample. When we look at the PETG, we also see the physical damage shown in Figure 5.6b. To avoid breaking the PETG, we stop applying strain.

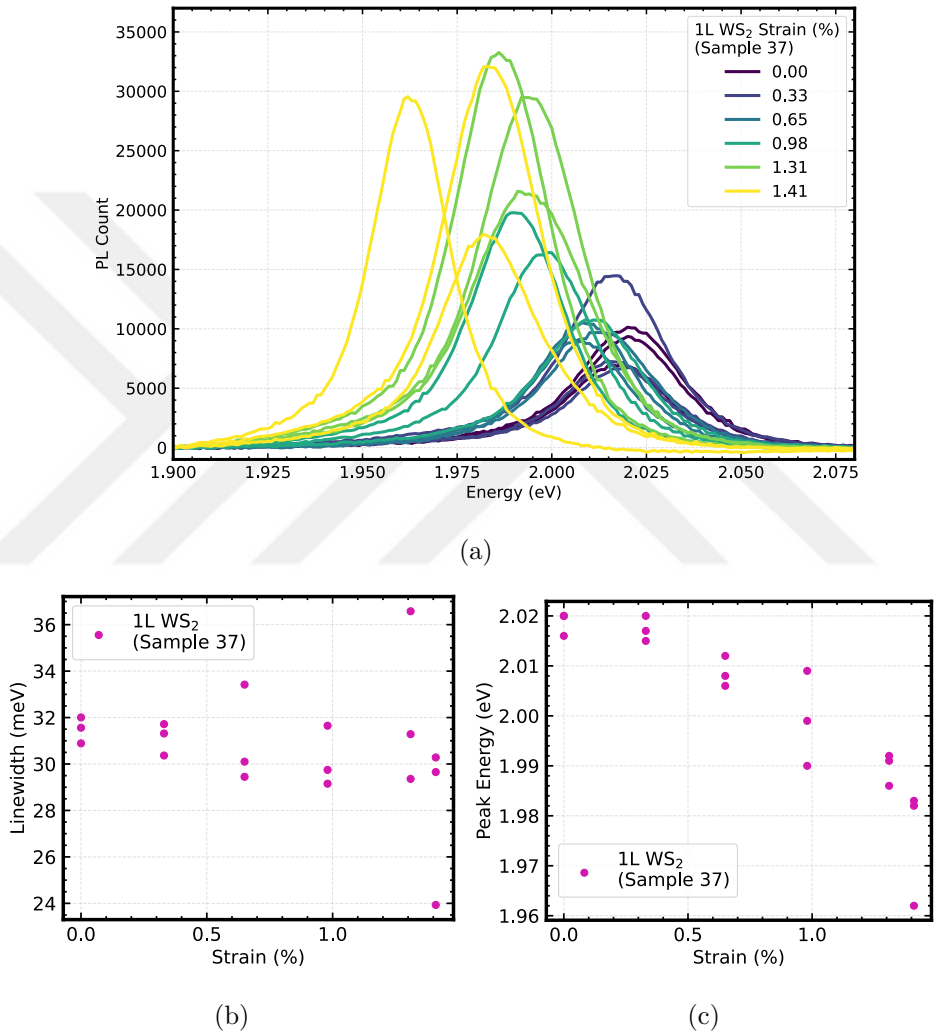

Figure 5.7. (a) PL spectra, (b) strain-dependent linewidth, (c) and peak energy analysis of the PL spectra of Sample 37 with the clamp width of 21 mm.

Another sample that we applied strain is Sample 37. In this sample, we started from a height of 9.20 mm and ended at 7.90 mm, with a decrement of 0.3 mm and a clamp width of 21 mm. We take measurements from the different locations within the same strain levels and observe different spectra for the same level, as shown in Figure 5.7a. When we analyze the features of the spectra, we see the redshift in the peak

position as Figure 5.7c, just like in Sample 33.

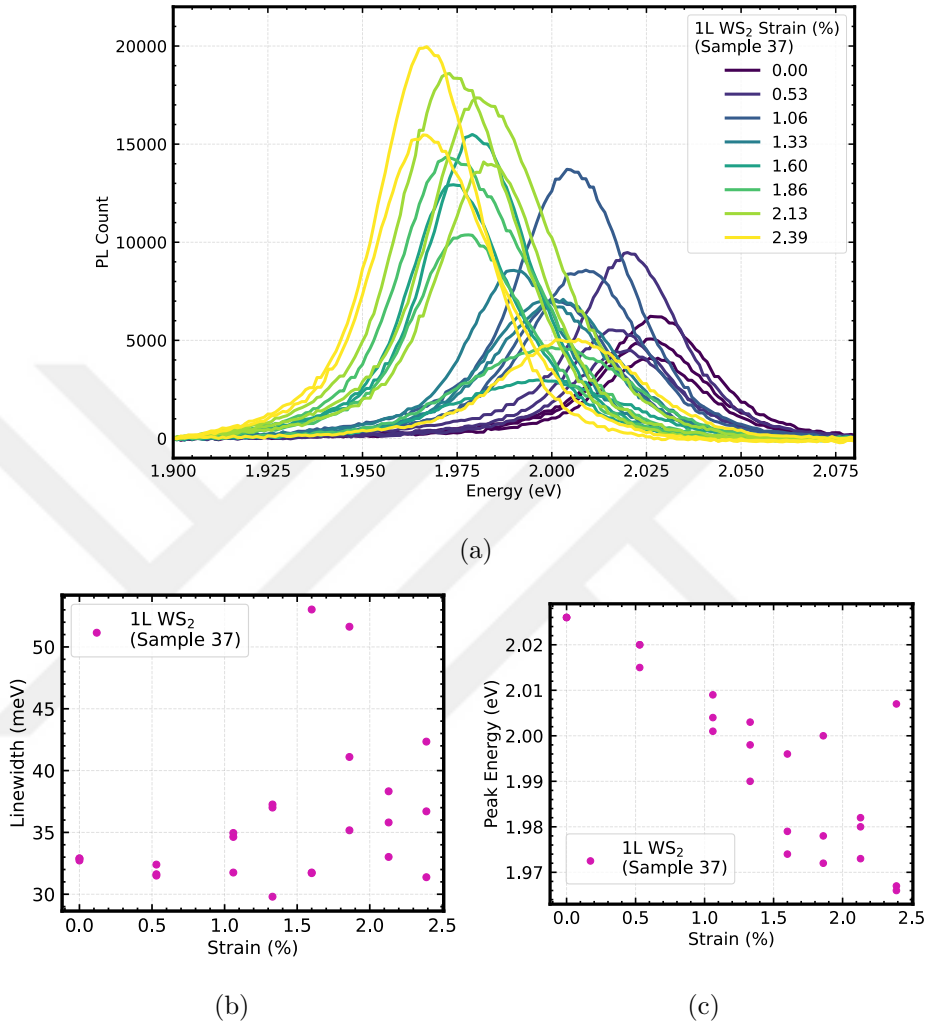

Figure 5.8. (a) PL spectra, (b) strain-dependent linewidth, (c) and peak energy analysis of the PL spectra of Sample 37 when the strain was applied the second time with the clamp width of 19 mm.

We observe a reverse correlation between linewidth and strain as shown in Figure 5.7b, but it is not trivial. Thus, just like Sample 33, we decide to apply strain a second time to Sample 37, keeping in mind that the maximum strain that is applied to Sample 33 was relatively low (0.77%) compared to Sample 37 (1.41%).

When the strain is applied a second time to Sample 37, we observe no trend when we analyze the linewidth of the PL spectra as presented in Figure 5.8b, and, except

for the low strain levels, there is no trend between peak position and strain, as Figure 5.8c illustrates. We interpret this as the strain we apply (1.41%) causes an irreversible change in 1L WS_2. There are wrinkles on the WS_2, and the strain is not transferred well.

Table 5.2. Statistics of the strain applied to 1L WS_2.

Sample	Clamp Width (mm)	Start (mm)	End (mm)	Max Strain (%)
33	37	9.20	7.00	0.77
33 (Second time)	18	9.00	7.40	2.37
37	21	9.20	7.90	1.41
37 (Second time)	19	9.10	7.30	2.39

5.3. Results

Several observations were made in our investigation of four strain experiments conducted on two different 1L WS_2 samples. Firstly, the strain does not propagate uniformly within the material, indicating variations in strain transfer efficiency across different regions. It was noted that points located further away from the bulk exhibit better strain transfer. Additionally, using a smaller clamp width improved the efficiency of the experiment. The effect of strain on 1L WS_2 was found to be reversible up to a certain extent, and when the strain exceeds approximately 2.30%, the material begins to crack, and strain transfer becomes ineffective.

6. STRAIN DEPENDENT NRET FROM QD TO WS_2

In this chapter, we investigate the effect of strain on the NRET rate between QDs and WS_2 through various experiments.

6.1. Coating the Surface with QD

From now on, the QDs mentioned are the CdSe/ZnS core-shell type QD from Sigma-Aldrich with $\lambda = 620$ nm $\pm$ 10 nm with the size of $\approx$ 4 nm and the procedures relating to diluting and dropping the QDs are done in the laboratory of Prof. Dr. Amitav Sanyal.

We fit Gaussian to the PL spectra and obtained the the peak of the QD as 608.9 nm, as shown in Figure 6.1.

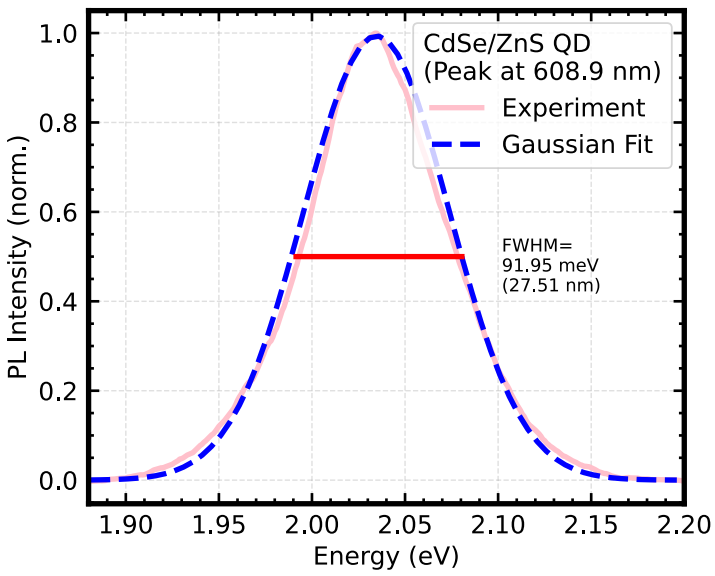

Figure 6.1. PL spectrum of the CdSe/ZnS QD.

We preferred water-soluble QD since toluene and ethanol disrupt the surface of the PETG, as depicted in Figure 6.2.

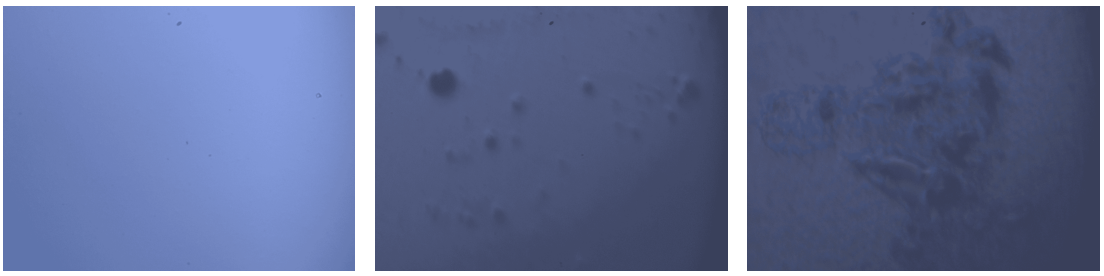

(a) (b) (c)

Figure 6.2. The surface of PETG: (a) bare, (b) ethanol dropped, (c) toluene dropped.

The QDs have a concentration of 1 mg/1 ml, which is too dense for our experiments. Thus, we dilute the QD to a concentration of about 0.01 mg/1 ml. Before dropping water-solved QD to WS_2, we first checked whether or not water moves the WS_2. For two different samples on PETG, we dropped distilled water and waited for it to dry. When comparing, we conclude that water does not cause movement on WS_2 on PETG, as shown in Figure 6.3.

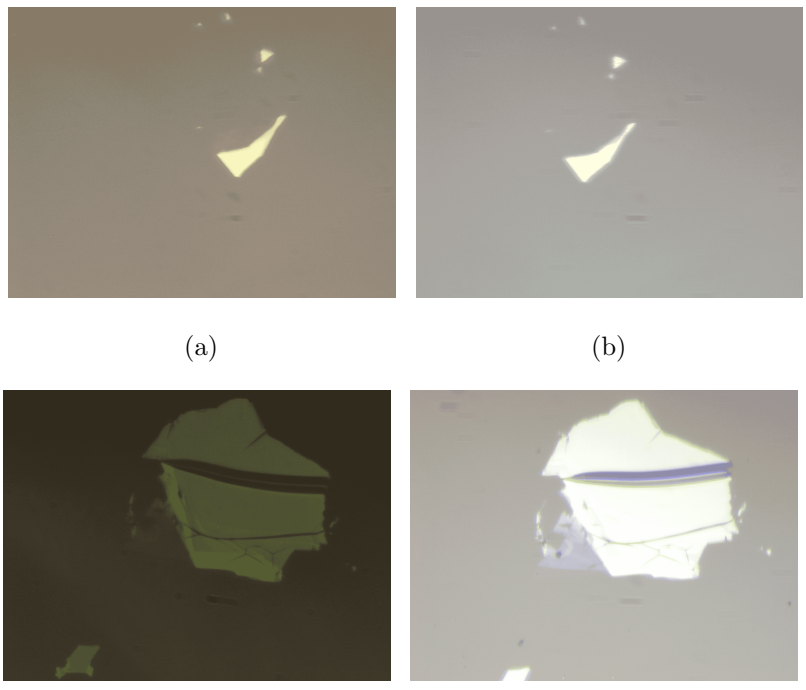

(a) (b)

(c) (d)

Figure 6.3. WS_2 flakes on PETG : (a,c) before, (b,d) after water is dropped.

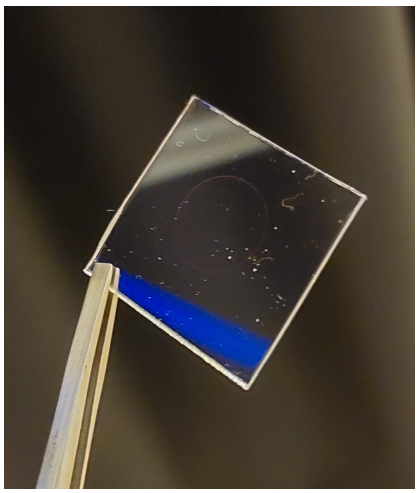

(a)

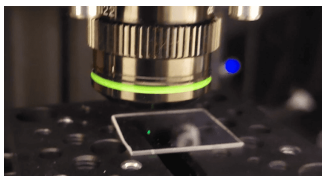

(b)

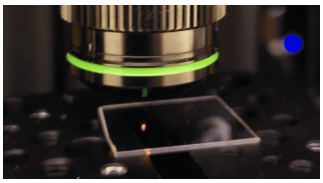

(c)

Figure 6.4. (a) Dried QD on PETG, (b) reflected laser from outside the QD circle, (c) from the outline of the circle.

The sizes of the PETG that we wanted to cover are too big to spin-coat, so instead, we drop 0.1 ml from the diluted QD to the surface of the PETG and then wait for water to dry overnight. After drying, we checked the surface PL to ensure QD dried homogeneously. Figure 6.4a shows the outline of the dried QDs, and except for the outline, the PL looks homogenous within the circle. PL is so strong on the outline that the green laser is not reflecting, as shown in Figure 6.4c. No PL exists outside the circle.

6.2. WS_2 on Top

We were unsure that QDs would dry evenly on top of WS_2 as they do on PETG surface. So, instead, we designate an area on the surface that contains QD to transfer the WS_2. During the transfer process, we noted that the surface was not as sticky as in the previous transfers, and some parts of the WS_2 were torn as shown in Figure 6.5. We transferred Sample 18, which contains both 1L and 2L regions.

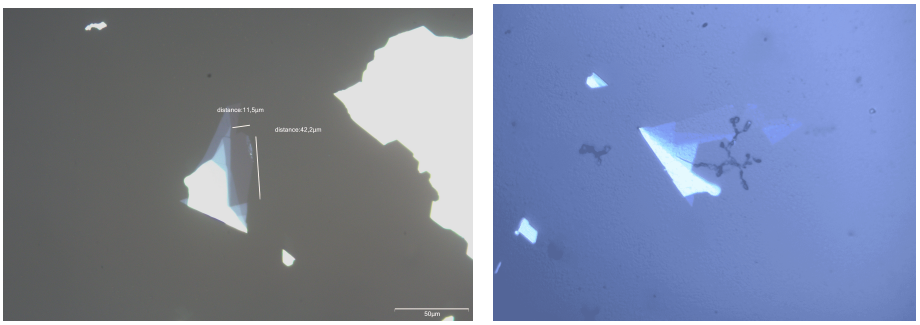

(a) (b)

Figure 6.5. Sample 18 is on: (a) PDMS before the transfer, (b) on PETG after the transfer.

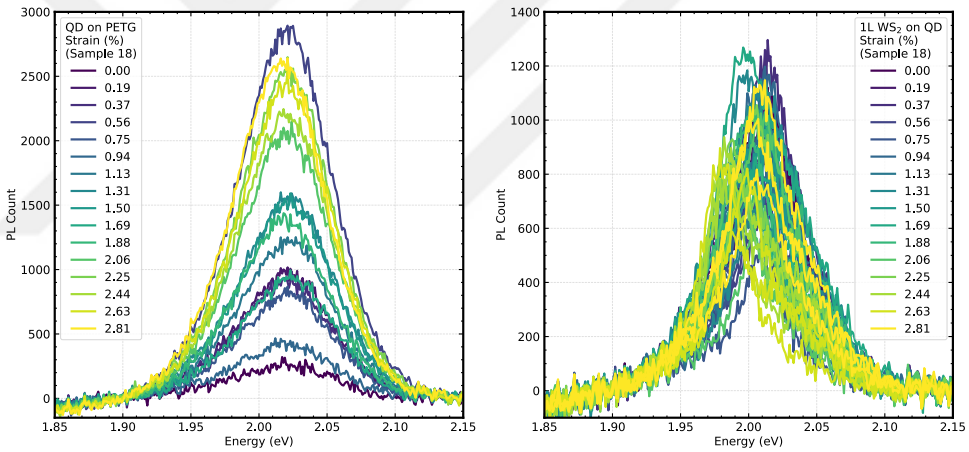

(a) (b)

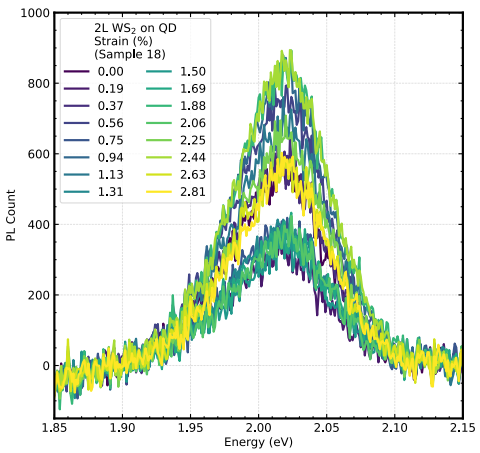

(c)

Figure 6.6. PL spectra of: (a) QD on PETG, (b) 1L WS_2 on QD, (c) 2L WS_2 on QD on Sample 18.

After transfer, we apply strain to Sample 18. We determine the height with 0% strain as 9.00 mm, and with the decrements of 0.10 mm, we lower the height to 7.60 mm with a clamp width of 17 mm. We take one measurement from the 2L WS_2 on QD since it is small and two or three measurements from 1L on QD WS_2 in the same strain level. We also get measurements from QD under strain. When we look at the PL spectra, we see no apparent dependence on the strain as presented in Figure 6.6.

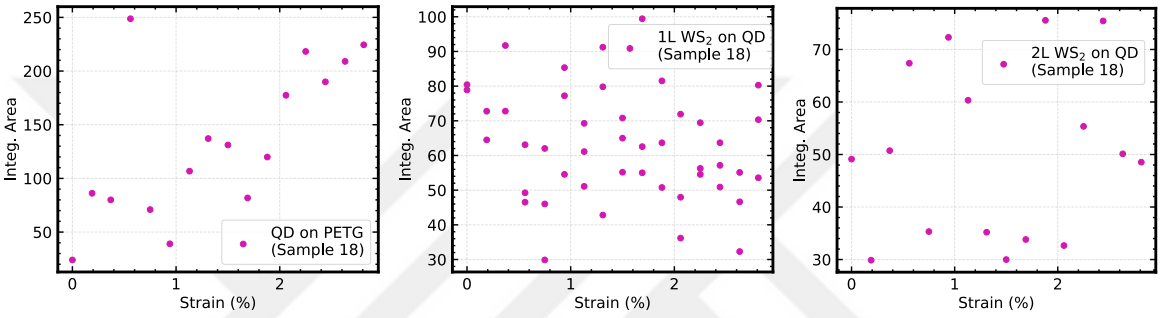

(a) (b) (c)

Figure 6.7. Strain-dependent integrated area of: (a) QD on PETG, (b) 1L WS_2 on QD, (c) 2L WS_2 on QD on Sample 18.

We look at the relation between the integrated area and the strain to get insight. Interestingly, for 1L WS_2 and 2L WS_2 on QD, we see no relation between strain and integrated area of the PL spectra as 6.7b and c. However, we detect a relation between strain and the PL spectra of the QD on PETG as shown in Figure 6.7a.

6.2.1. Strain-dependent PL Spectra of the QD

To ensure the relation between strain and integrated PL area is not a coincidence or caused because when taking the data, we did not measure from the same QD point, we repeat the strain experiment. We use Sample 18 again since strain should not have a structural effect on QD, unlike WS_2. We locate two points, Point 1 and Point 2, that PL is bright as depicted in Figure 6.8. We note the positions of these points, and try to take the measurements as much as possible at the same place.

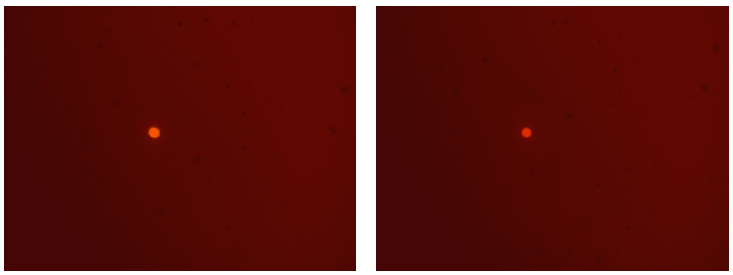

(a) (b)

Figure 6.8. PL from: (a) Point 1, (b) Point 2.

When we analyze the PL spectra of Point 1 and Point 2, we see no correlation under strain, as demonstrated in Figure 6.9, suggesting the strain-dependent nature of the QDs is just a coincidence and possibly resulted from data taken in different locations.

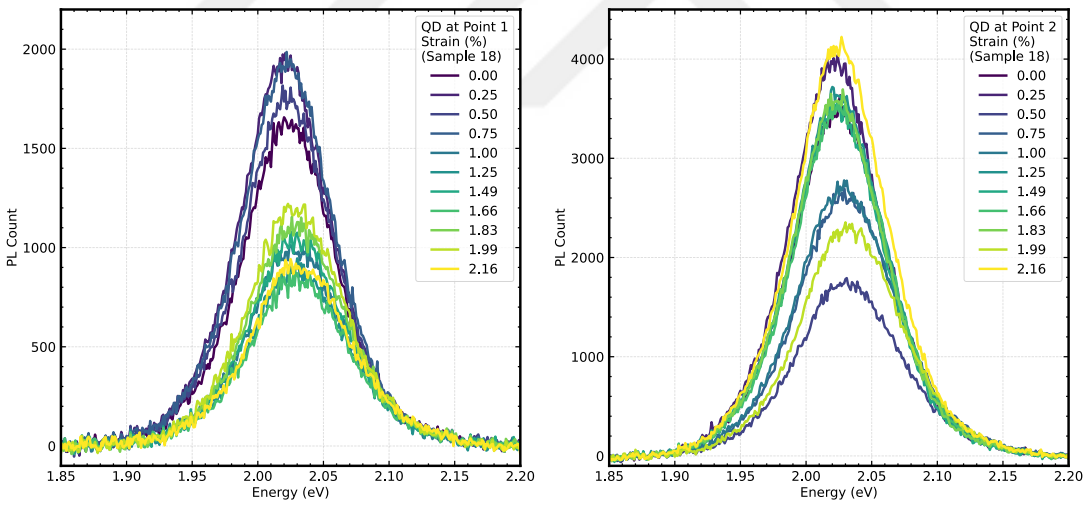

(a) (b)

Figure 6.9. Strain-dependent spectra of QD: (a) Point 1, (b) Point 2.

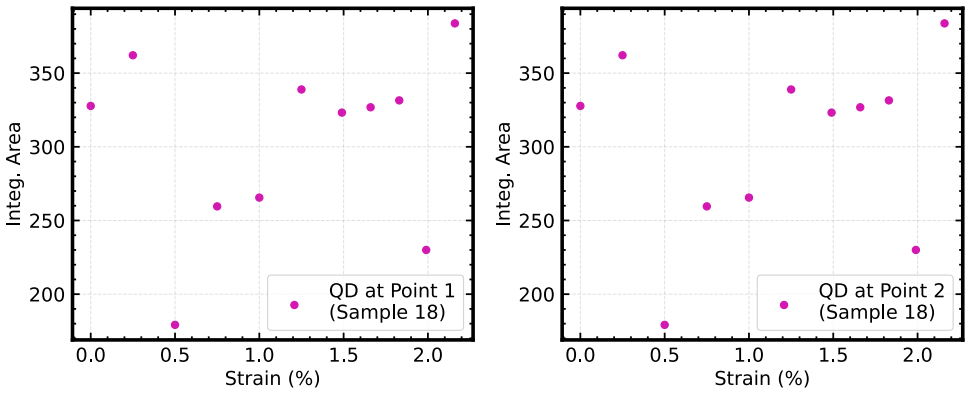

(a) (b)

Figure 6.10. Strain-dependent integrated area of PL spectra: (a) Point 1, (b) Point 2.

6.3. QD on Top

6.3.1. PL Measurements

We suspect that the reason for not observing a strain dependence in the PL spectra of Sample 18 is that when QDs are on the bottom, and they do not excite properly. So, instead, we first transfer the WS_2 to PETG and dry the QD after the transfer for Sample 27.

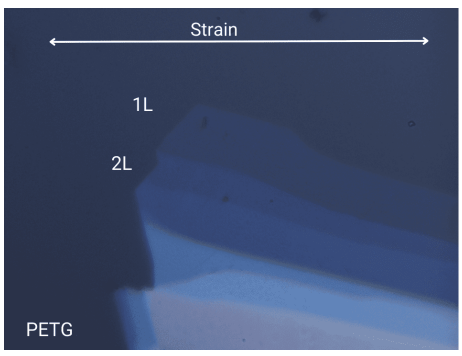

Figure 6.11. Sample 27 on the PETG, double arrow shows the direction of the applied strain.

We determined the height with 0% strain as 9.00 mm, and we lowered the height to 7.65 mm with a clamp width of 18 mm. We take one measurement from the QD on 2L WS_2 since it is small and three measurements from QD on 1L WS_2 in the same

strain level. We also, get measurements from QD on PETG under strain as shown in Figure 6.12.

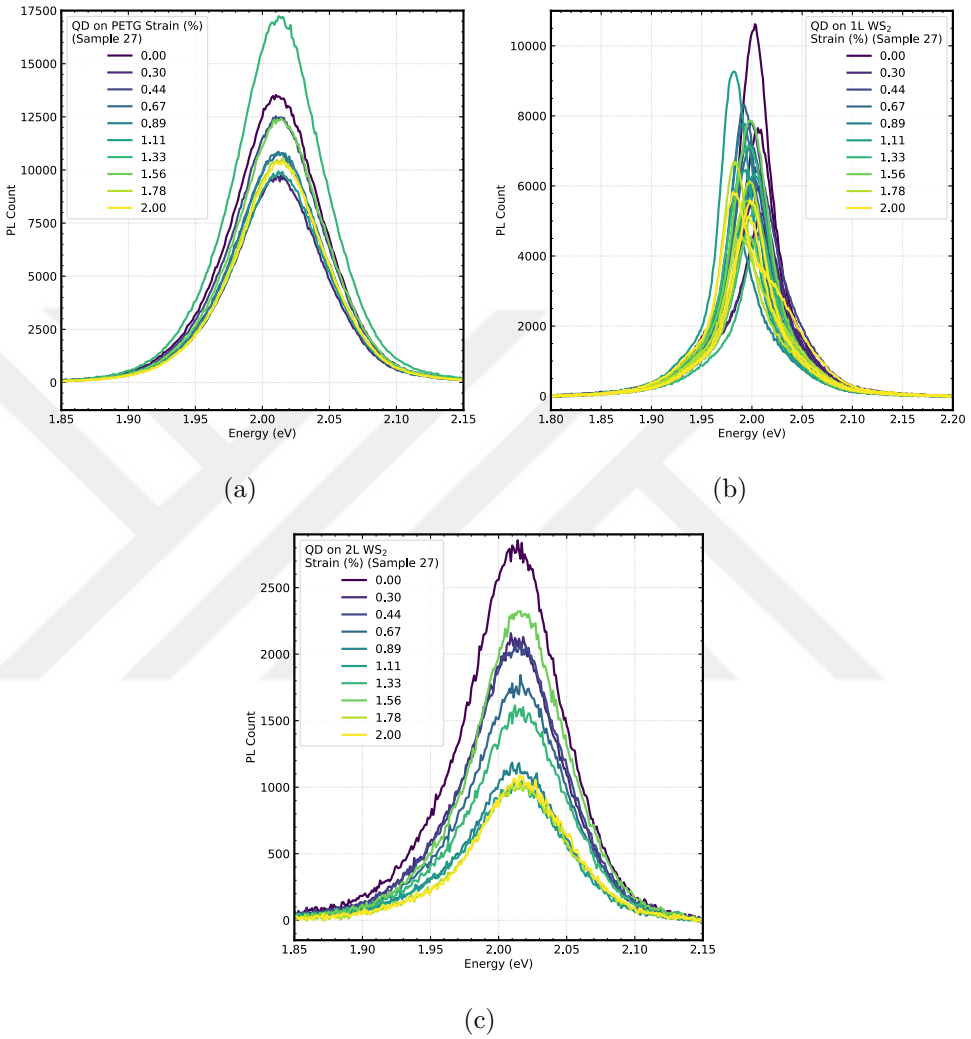

Figure 6.12. Strain-dependent PL spectra of QD on: (a) PETG, (b) 1L WS_2, (c) 2L WS_2 on Sample 27.

When we analyze the PL spectra, we see no apparent relation with strain for the integrated area for the QD on 1L WS_2 as displayed in Figure 6.13b. This is no surprise since the PL from 1L WS_2 is comparable to PL from QD, just like we stated before, and when we look at the PL spectra of this system, we see the combined count coming from both QD and 1L WS_2. We can observe this combination with increasing strain since with strain, there is a red shift in the peak of 1L WS_2. We see a split in the peak under strain as displayed in Figure 6.12b. Interestingly, for the QD on 2L WS_2,

we find a decrease in PL with strain as shown in Figure 6.13c. Decreased PL suggests increased NRET, which contradicts the theoretically calculated relation.

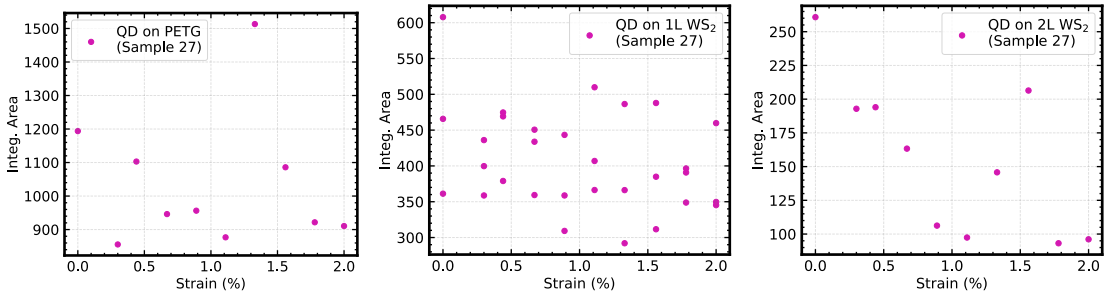

(a) (b) (c)

Figure 6.13. Strain-dependent integrated area under PL spectra of QD: on (a) PETG, (b) 1L WS_2, (c) 2L WS_2 on Sample 27.

When we further investigate the effect of strain on the material, we realize that, under strain, the electric field on the interface also changes. Near the energy level of interest (2 eV), there is a decrease in electric field intensity $|E|^2$ as presented in Figure 6.14 due to the absorption by the 2D material. Therefore, we cannot confidently attribute the decrease in the integrated area under the PL spectra solely to strain. A reduction in $|E|^2$ due to strain is expected to cause a decrease in PL intensity.

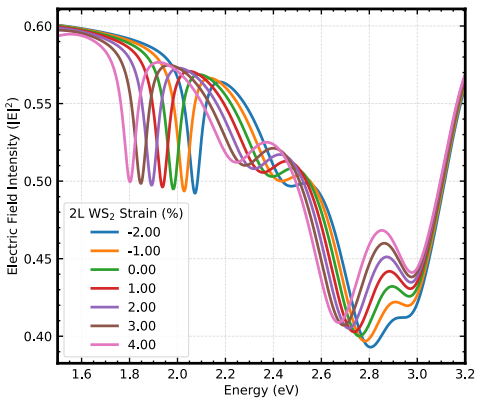

Figure 6.14. Strain-dependent electric field intensity relative to the incident intensity on the surface of 2L WS_2 on PETG.

To get around these effects and better observe the effect of strain on the system, we decided to perform TRPL measurements where we can get the decay rates.

6.3.2. TRPL Measurements

We perform TRPL measurements in the Bilkent University UNAM Center. In their setup, we applied strain to the hybrid structure of QD on 2L WS_2 on Sample 41 as presented in Figure 6.15 using a 10 MHz pulsed laser with 1.1 mW power. As we stated before, the strain does not transmit equally on the surface, so we took measurements at two different points in 2L WS_2 at the same strain level to ensure we applied strain. Before applying strain, we took lifetime measurements from QD on the PETG and QD on bulk WS_2.

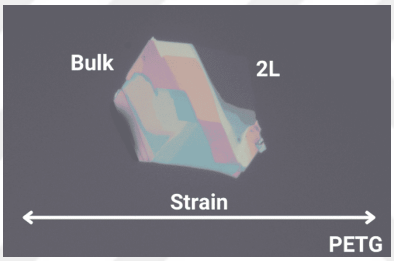

Figure 6.15. Sample 41 on PETG, double arrow shows the direction of the applied strain.

As noise power, we choose 0.50 since the higher values smooth the data and information is lost, and with lower values, the noise is too much for analyzing, as displayed in Figure 6.16.

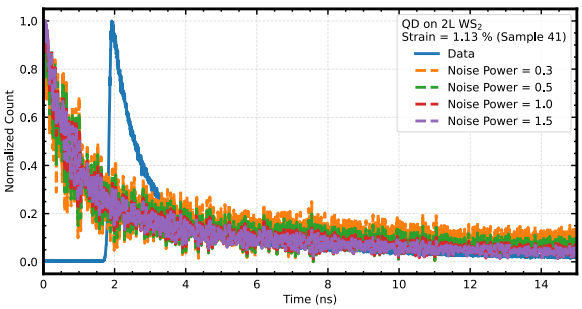

Figure 6.16. Different decays obtained with different noise power values to wiener deconvolution.

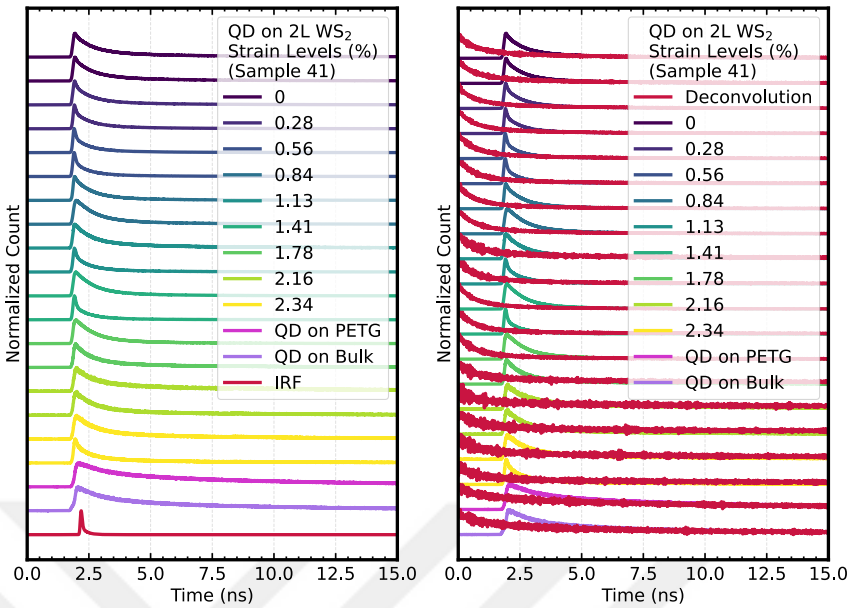

(a) (b)

Figure 6.17. (a) Normalized count of the data taken from Sample 41, (b) deconvolution of the TRPL data together with normalized data for comparison.

Figure 6.17a shows the normalized TRPL data that we take and the IRF of the system, Figure 6.17b shows the deconvoluted and the normalized data together.

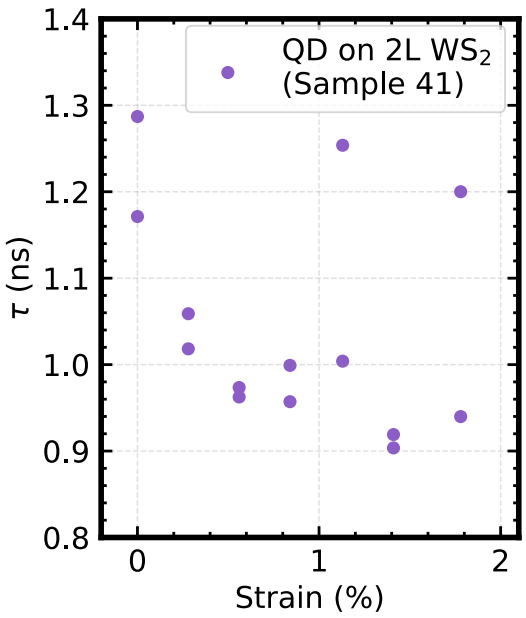

Figure 6.18. Lifetimes obtained by making exponential fits to deconvoluted data as a function of strain.

After doing analysis and exponential fitting data, we obtain the lifetime values. As shown in Figure 6.18, there are different lifetime values for the same strain levels. As we stated before, the strain does not transfer equally along the surface, and there could be different spectra for the same strain level.

6.4. Results and Discussion

To summarize this section, we were able to apply uniaxial strain to the QD and WS_2 system and tune the NRET rate. From our TRPL experiments, we find the lifetime of the excitons in QD on PETG is 3.24 ns, longer than the lifetime of the excitons in QD on 2L WS_2 at any strain level. Thus, we can say there is NRET from QD to 2L WS_2. And, since the lifetime of the excitons in QD on 2L WS_2 decreases with strain, as presented in Figure 6.18, the QD excitons decay into 2L WS_2 nonradiatively faster under strain, and NRET becomes more efficient.

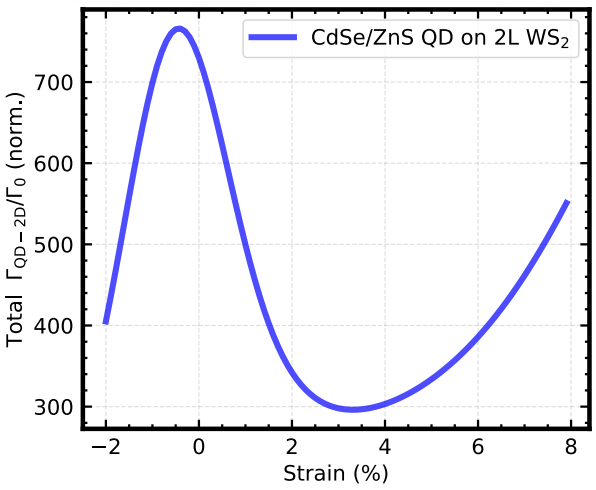

Figure 6.19. Total NRET rate between CdSe/ZnS QD and 2L WS_2 as a function of strain.

Additionally, since TRPL measurements provide insights into decay rates, the observed decrease in the integrated area under PL spectra of QD on 2L WS_2, as shown in Figure 6.13c, can also be attributed to strain, further suggesting an increase in the NRET rate. However, when we follow the steps described in Section 2.1, assuming same strain-dependence applies for 2L WS_2, for the CdSe/ZnS QD and 2L WS_2, theoretical

predictions indicate a decrease in the NRET rate with to strain, as presented in Figure 6.19, suggesting a disagreement between between theory and the result of experiments. Nevertheless, our experiments are limited and insufficient to comment on the theory's validity.

7. THICKNESS DEPENDENT NRET FROM QD TO WS_2

This chapter investigates the NRET rate from QD on 2L WS_2 and bulk WS_2.

7.1. TRPL Measurements

In Sample 41, before taking strain-dependent TRPL measurements, we got measurements from the QD on PETG, 2L, and bulk WS_2 as displayed in Figure 6.17. We obtain the lifetimes by analyzing the data from the measurements and making the exponential fits. The lifetime of the excitons in QD on PETG is 3.24 ns, on 2L WS_2 0.78 ns and on bulk WS_2, it is 2.64 ns as illustrated in Figure 7.1.

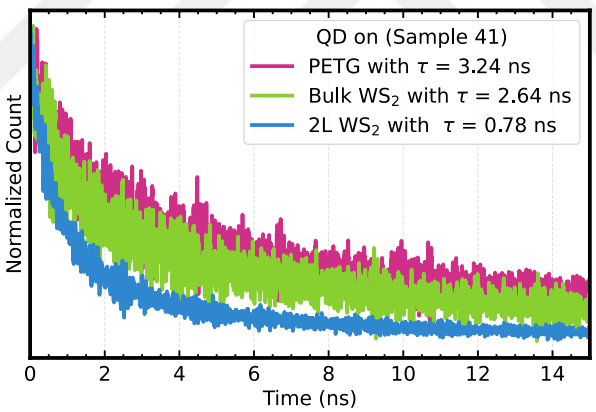

Figure 7.1. Comparing the lifetime of the excitons in QD on PETG, 2L WS_2 and bulk WS_2 on Sample 41.

7.2. PL Mapping

One of our main concerns was that since we dry QD overnight instead of spin-coating, they are not homogeneous on the surface or WS_2. Thus, we dried QD on Sample 39 which contains WS_2 flake as presented in Figure 7.2, and performed PL mapping to QD on PETG and QD on 2L WS_2 with 10 μm $\times$ 10 μm area with 0.2 μm steps with an objective with resolution of 0.7 μm.



Figure 7.2. Sample 39 on PETG.

To analyze the data from PL mapping, we follow the same procedure for the PL analysis (except for the efficiency correction). We are mainly interested in the peak and the linewidth of the PL spectra with the integrated area under the PL spectra of QD on PETG and 2L WS_2.

As illustrated in Figure 7.3a, QD dried on PETG surface rather evenly. As for QD on 2L WS_2, they seem to cluster as shown in Figure 7.3b. The reason for the clustering behavior is outside the scope of this thesis.

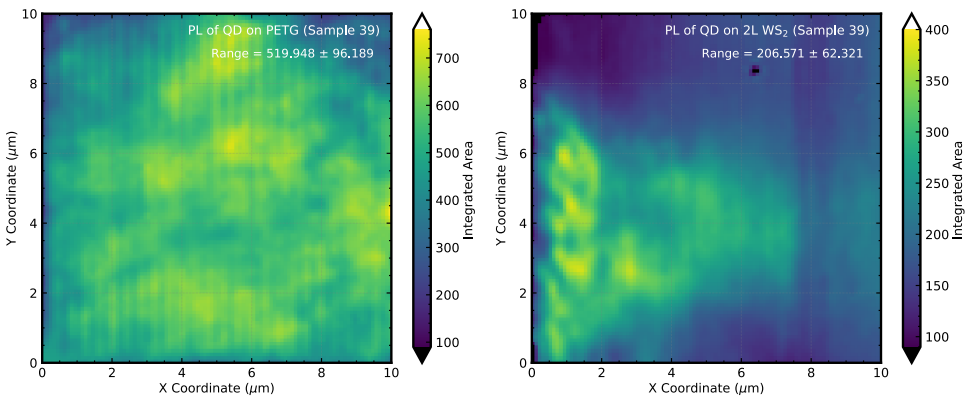

(a) (b)

Figure 7.3. Heatmap of the integrated areas of the PL spectra of QD on: (a) PETG, (b) 2L WS_2.

When further investigating Figure 7.3, we see that the range of the integrated areas of the PL spectra of QD on PETG (≈ 520) is more than twice the mean value

of QD on 2L WS_2 ($\approx$ 206).

We would like to note that since the electric field intensity on the surface of PETG is higher, the PL should be higher on the surface of PETG as shown in Figure 7.4. However, since we did TRPL measurements and calculated the decay rates of QD on PETG and 2L WS_2 as presented in Figure 7.1, we attribute the decreased PL to NRET from QD to 2L WS_2.

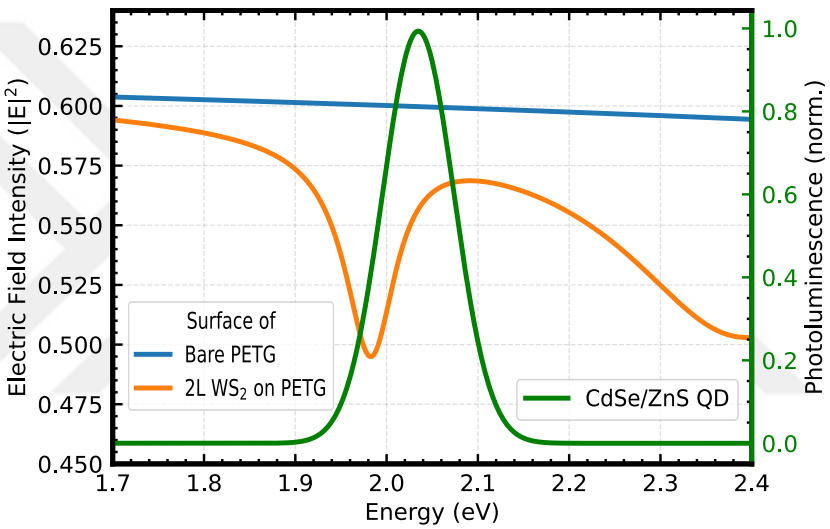

Figure 7.4. Electric field intensity relative to the incident intensity on the surface of PETG and 2L WS_2, PL spectra of QD to compare.

When we examine the PL spectra of QD on PETG and 2L WS_2, we observe that the QD exhibits the same mean emission peak ($\approx$ 2.02 eV) with a comparably small standard deviation on both surfaces, as shown in Figure 7.5a and b. Additionally, the linewidth of the PL spectra on both surfaces falls within a similar range ($\approx$ 78 meV), as depicted in Figure 7.5c and d.

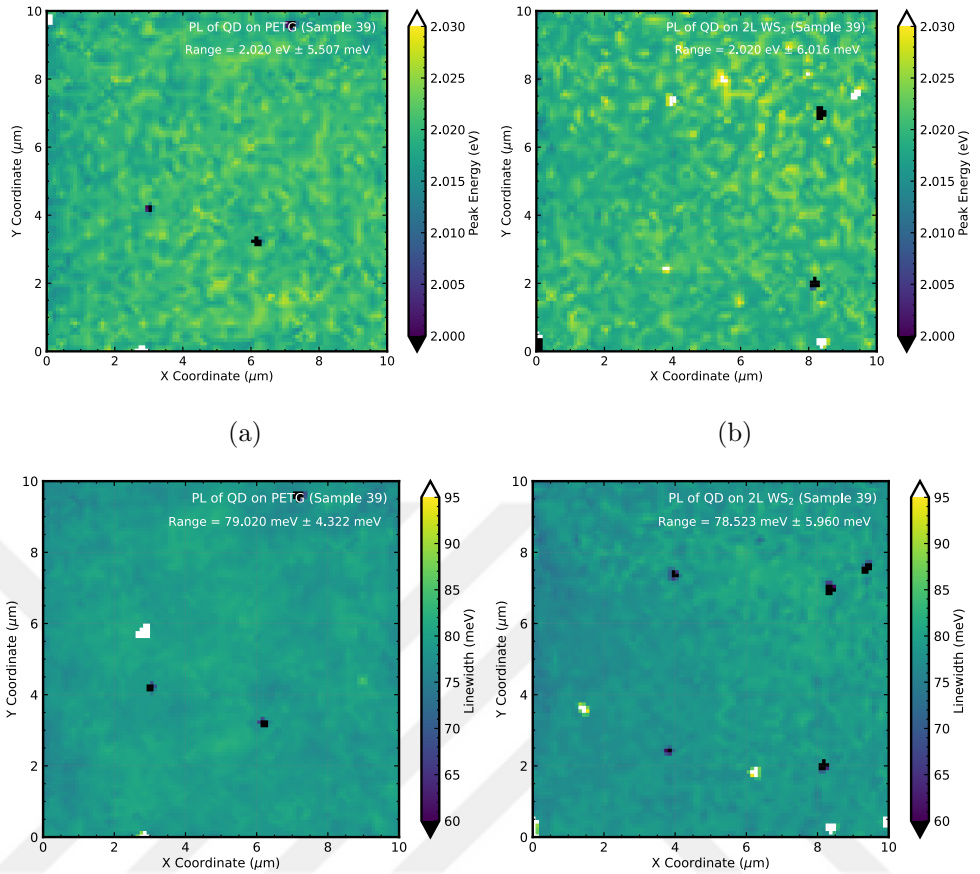

Figure 7.5. Heatmap of the peak energy of the PL spectra of (a) QD on PETG, (b) QD on 2L WS_2. Heatmap of the linewidth of the PL spectra of (c) QD on PETG, (d) QD on 2L WS_2.

7.3. Results and Discussion

In the TMCDs, an increase in the dielectric screening with the thickness is reported as Figure 7.6 illustrates. In our TRPL experiments, we were able to show the effect of dielectric screening on the NRET. As Figure 7.1 displays, the QD excitons' lifetime is shorter on 2L and bulk WS_2 compared to the lifetime of the excitons in the QDs on PETG suggesting a nonradiative decay into WS_2. The shorter lifetime on 2L WS_2 implies that the NRET is more efficient to 2L WS_2 than to bulk WS_2.

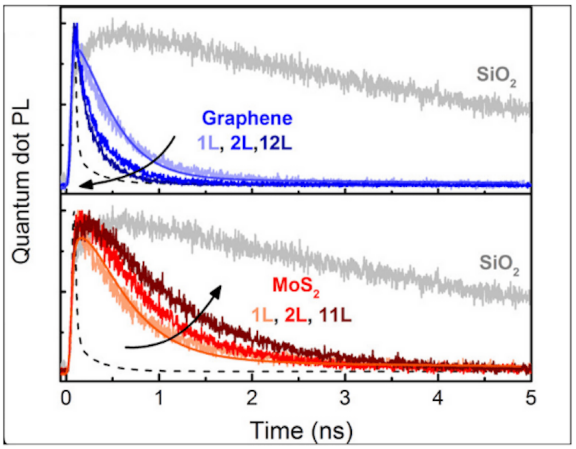

Figure 7.6. TRPL traces on graphene layers are shown in the top panel and on MoS_2 in the bottom panel. Exemplary fits are overlaid on the data in solid blue and red lines. The gray trace corresponds to the SiO_2 substrate, and the instrument response function is the dashed black line taken from [66].

8. CONCLUSION

In a system where both radiative and nonradiative processes (such as NRET) exist, the observed decay rate is the combined decay rate of both processes. When we measure the PL, we see the radiative process. Thus, the decrease in the PL spectra suggests that the non-radiative decay channels are more prominent and NRET is preferred. More efficient NRET means there are more pathways for excitons. They spend less time in their excited states, resulting in a shorter lifetime. Therefore, by performing TRPL experiments, we can comment on the efficiency of the NRET rate.

Before conducting the experiments, we theoretically calculated the NRET rate as a function of strain, providing us with a basis for our expectations. When the strain is applied, the overlap between emission and absorption spectra decreases, making the NRET less efficient with strain, as shown in Figure 2.7.

To investigate the relation between NRET and strain, we performed PL and TRPL measurements. We applied strain to 2D materials in a three-point bending geometry on PETG substrates. Our strain-dependent PL experiments reveal a decrease in the integrated area under the PL spectra with strain, as depicted in Figure 6.13c, suggesting that the NRET becomes more prominent with strain. Additionally, from the TRPL measurements, we find a decrease in the lifetime of the excitons in QD on 2L WS_2 via strain, corresponding to an increase in the NRET rate as shown in Figure 6.18. Both of these experiments suggest that the NRET rate increases with increasing strain, contrasting with theory.

We also investigate the relation between thickness and NRET rate. Our TRPL experiments showed that the lifetime of the excitons in the QD on 2L WS_2 (0.78 ns) and on bulk WS_2 (2.64 ns) is shorter than QD on PETG (3.24 ns). This difference in the lifetime values implies two things. First, there is a non-radiative decay happening from QD to WS_2, and second, the NRET into 2L WS_2 is more efficient than into bulk.

Both of these findings align with the literature.

We can also see the evidence of NRET in the PL mapping experiments as depicted in Figure 7.3. When PL from QD on PETG and PL from QD on 2L WS_2 is compared, there is significant quenching of the PL of QD on 2L due to NRET.

While our experiments suggest a behavior opposite to the theory, it's essential to conduct additional experiments. These further investigations will provide the necessary data to confirm the observed differences or adjust the theoretical framework to match our findings better. These further investigations will provide the necessary data to confirm the observed differences or adjust the theoretical framework to appropriately.

REFERENCES

1. Chance, R., A. Prock and R. Silbey, "Molecular Fluorescence and Energy Transfer Near Interfaces", *The Journal of Chemical Physics*, Vol. 37, pp. 2527–2534, 1978.

2. Lakowicz, J. R., *Principles of Fluorescence Spectroscopy*, Springer, New York, 2013.

3. Agranovich, V. and M. Galanin, *Electronic Excitation Energy Transfer in Condensed Matter*, North-Holland Publishing Company, Holland, 1982.

4. Guzelturk, B. and H. V. Demir, "Near-Field Energy Transfer Using Nanoemitters For Optoelectronics", *Advanced Functional Materials*, Vol. 26, No. 45, pp. 8158–8177, 2016.

5. Achermann, M., M. A. Petruska, S. Kos, D. L. Smith, D. D. Koleske and V. I. Klimov, "Energy-Transfer Pumping of Semiconductor Nanocrystals Using an Epitaxial Quantum Well", *Nature*, Vol. 429, No. 6992, pp. 642–646, 2004.

6. Erdem, O., K. Gungor, B. Guzelturk, I. Tanriover, M. Sak, M. Olutas, D. Dede, Y. Kelestemur and H. V. Demir, "Orientation-Controlled Nonradiative Energy Transfer to Colloidal Nanoplatelets: Engineering Dipole Orientation Factor", *Nano Letters*, Vol. 19, No. 7, pp. 4297–4305, 2019.

7. Hillisch, A., M. Lorenz and S. Diekmann, "Recent Advances in FRET: Distance Determination in Protein–DNA Complexes", *Current Opinion in Structural Biology*, Vol. 11, No. 2, pp. 201–207, 2001.

8. Medintz, I. L., A. R. Clapp, H. Mattoussi, E. R. Goldman, B. Fisher and J. M. Mauro, "Self-Assembled Nanoscale Biosensors Based on Quantum Dot FRET Donors", *Nature Materials*, Vol. 2, No. 9, pp. 630–638, 2003.

9. Chang, H., L. Tang, Y. Wang, J. Jiang and J. Li, "Graphene Fluorescence Reso-

nance Energy Transfer Aptasensor for the Thrombin Detection", *Analytical Chemistry*, Vol. 82, No. 6, pp. 2341–2346, 2010.

10. Şimşek, E. and B. Aslan, "Computing Strain-Dependent Energy Transfer from Quantum Dots to 2D Materials", *Nano Futures*, Vol. 7, No. 2, pp. 1–7, 2023.

11. Novoselov, K. S., D. Jiang, F. Schedin, T. J. Booth, V. V. Khotkevich, S. V. Morozov and A. K. Geim, "Two-Dimensional Atomic Crystals", *Proceedings of the National Academy of Sciences*, Vol. 102, No. 30, pp. 10451–10453, 2005.

12. Dickinson, R. G. and L. Pauling, "The Crystal Structure of Molybdenite", *Journal of the American Chemical Society*, Vol. 45, No. 6, pp. 1466–1471, 1923.

13. Frindt, R. F. and A. D. Yoffe, "Optical Properties and Photoconductivity of Thin Crystals of Molybdenum Disulphide", *Proceedings of the Royal Society of London Series A. Mathematical and Physical Sciences*, Vol. 273, No. 1352, pp. 69–83, 1963.

14. Mak, K. F., C. Lee, J. Hone, J. Shan and T. F. Heinz, "Atomically Thin MoS_2: A New Direct-Gap Semiconductor", *Physical Review Letters*, Vol. 105, No. 13, pp. 1–4, 2010.

15. Radisavljevic, B., A. Radenovic, J. Brivio, V. Giacometti and A. Kis, "Single-Layer MoS_2 Transistors", *Nature Nanotechnology*, Vol. 6, No. 3, pp. 147–150, 2011.

16. McDonnell, S. J. and R. M. Wallace, "Atomically-Thin Layered Films for Device Applications Based Upon 2D TMDC Materials", *Thin Solid Films*, Vol. 616, pp. 482–501, 2016.

17. Wang, Q. H., K. Kalantar-Zadeh, A. Kis, J. N. Coleman and M. S. Strano, "Electronics and Optoelectronics of Two-Dimensional Transition Metal Dichalcogenides", *Nature Nanotechnology*, Vol. 7, No. 11, pp. 699–712, 2012.

18. Wu, W., L. Wang, Y. Li, F. Zhang, L. Lin, S. Niu, D. Chenet, X. Zhang, Y. Hao,

T. F. Heinz, J. Hone and Z. L. Wang, "Piezoelectricity of Single-Atomic-Layer MoS_2 for Energy Conversion and Piezotronics", *Nature*, Vol. 514, No. 7523, pp. 470–474, 2014.

19. Manzeli, S., D. Ovchinnikov, D. Pasquier, O. V. Yazyev and A. Kis, "2D Transition Metal Dichalcogenides", *Nature Reviews Materials*, Vol. 2, pp. 1–15, 2017.

20. Xiao, D., G.-B. Liu, W. Feng, X. Xu and W. Yao, "Coupled Spin and Valley Physics in Monolayers of MoS_2 and Other Group-VI Dichalcogenides", *Physical Review Letters*, Vol. 108, No. 19, pp. 1–5, 2012.

21. Awan, S. U., S. Zainab, M. D. Khan, S. Rizwan and M. Z. Iqbal, "2-Dimensional Magnetic Materials for Spintronics Technology", *The Royal Society of Chemistry*, Vol. 6, pp. 91–119, 2020.

22. Yun, W. S., S. W. Han, S. C. Hong, I. G. Kim and J. D. Lee, "Thickness and Strain Effects on Electronic Structures of Transition Metal Dichalcogenides: 2H-MX_2 Semiconductors (M = Mo, W; X = S, Se, Te)", *Physical Review B*, Vol. 85, No. 3, pp. 1–5, 2012.

23. Ruat, M., E. G. d'Aillon and L. Verger, "3D Semiconductor Radiation Detectors for Medical Imaging: Simulation and Design", *2008 IEEE Nuclear Science Symposium Conference Record*, pp. 434–439, Dresden, Germany, 2008.

24. Hulicius, E. and V. Kubeček, *Semiconductor Lasers for Medical Applications*, Woodhead Publishing, United Kingdom, 2013.

25. Chhowalla, M., D. Jena and H. Zhang, "Two-Dimensional Semiconductors for Transistors", *Nature Reviews Materials*, Vol. 1, No. 11, pp. 16–52, 2016.

26. Woggon, U., *Optical Properties of Semiconductor Quantum Dots*, Springer, Berlin, 1997.

27. Chen, J., V. Hardev and J. Yurek, "Quantum-Dot Displays: Giving LCDs a Competitive Edge Through Color", *Frontline Technology*, Vol. 29, No. 1, pp. 12–17, 2013.

28. Davies, C. T. H. and A. C. L. Wong, *Quantum Dots: A Doorway to Nanoscale Physics*, Springer, Berlin, 2024.

29. de Arquer, F. P. G., D. V. Talapin, V. I. Klimov, Y. Arakawa, M. Bayer and E. H. Sargent, "Semiconductor Quantum Dots: Technological Progress and Future Challenges", *Science*, Vol. 373, No. 6555, pp. 1–14, 2021.

30. Rogach, A. L., *Semiconductor Nanocrystal Quantum Dots*, Springer, Berlin, 2008.

31. Wang, L., L. Huang, W. C. Tan, X. Feng, L. Chen, X. Huang and K.-W. Ang, "2D Photovoltaic Devices: Progress and Prospects", *Small Methods*, Vol. 2, No. 3, pp. 1–20, 2018.

32. Özdemir, O., I. Ramiro, S. Gupta and G. Konstantatos, "High Sensitivity Hybrid PbS CQD-TMDC Photodetectors up to 2 μm", *ACS Photonics*, Vol. 6, No. 10, pp. 2381–2386, 2019.

33. Zhang, L., K. Gong, J. Chen, L. Liu, Y. Zhu, D. Xiao and H. Guo, "Generation and Transport of Valley-Polarized Current in Transition-Metal Dichalcogenides", *Physical Review B*, Vol. 90, No. 19, pp. 1–7, 2014.

34. Chernikov, A., A. M. van der Zande, H. M. Hill, A. F. Rigosi, A. Velauthapillai, J. Hone and T. F. Heinz, "Electrical Tuning of Exciton Binding Energies in Monolayer WS_2", *Physical Review Letters*, Vol. 115, No. 12, pp. 1–6, 2015.

35. Prasai, D., A. R. Klots, A. Newaz, J. S. Niezgoda, N. J. Orfield, C. A. Escobar, A. Wynn, A. Efimov, G. K. Jennings, S. J. Rosenthal and K. I. Bolotin, "Electrical Control of Near-field Energy Transfer Between Quantum Dots and Two-dimensional Semiconductors", *Nano Letters*, Vol. 15, No. 7, pp. 4374–4380, 2015.

36. Younas, R., G. Zhou and C. L. Hinkle, "A Perspective on the Doping of Transition Metal Dichalcogenides for Ultra-Scaled Transistors: Challenges and Opportunities", *Applied Physics Letters*, Vol. 112, No. 16, pp. 1–12, 2023.

37. Waldecker, L., A. Raja, M. Rösner, C. Steinke, A. Bostwick, R. J. Koch, C. Jozwiak, T. Taniguchi, K. Watanabe, E. Rotenberg, T. O. Wehling and T. F. Heinz, "Rigid Band Shifts in Two-Dimensional Semiconductors Through External Dielectric Screening", *Physical Review Letters*, Vol. 123, No. 20, pp. 1–6, 2019.

38. Borghardt, S., J.-S. Tu, F. Winkler, J. Schubert, W. Zander, K. Leosson and B. E. Kardynał, "Engineering of Optical and Electronic Band Gaps in Transition Metal Dichalcogenide Monolayers Through External Dielectric Screening", *Physical Review Materials*, Vol. 1, No. 5, pp. 1–8, 2017.

39. Ma, X., N. Youngblood, X. Liu, Y. Cheng, P. Cunha, K. Kudtarkar, X. Wang and S. Lan, "Engineering Photonic Environments for Two-Dimensional Materials", *Nanophotonics*, Vol. 10, No. 3, pp. 1031–1048, 2021.

40. Ma, X., K. Kudtarkar, Y. Chen, P. Cunha, Y. Ma, K. Watanabe, T. Taniguchi, X. Qian, M. C. Hipwell, Z. J. Wong and S. Lan, "Coherent Momentum Control of Forbidden Excitons", *Nature Communications*, Vol. 13, pp. 1–9, 2022.

41. Desai, S. B., G. Seol, J. S. Kang, H. Fang, C. Battaglia, R. Kapadia, J. W. Ager, J. Guo and A. Javey, "Strain-Induced Indirect to Direct Bandgap Transition in Multilayer WSe_2", *Nano Letters*, Vol. 14, No. 8, pp. 4592–4597, 2014.

42. Aslan, B., I. M. Datye, M. J. Mleczko, K. Sze Cheung, S. Krylyuk, A. Bruma, I. Kalish, A. V. Davydov, E. Pop and T. F. Heinz, "Probing the Optical Properties and Strain-Tuning of Ultrathin $Mo_{1-x}W_xTe_2$", *Nano Letters*, Vol. 18, No. 4, pp. 2485–2491, 2018.

43. Aslan, B., M. Deng, M. L. Brongersma and T. F. Heinz, "Strained Bilayer WSe_2

with Reduced Exciton-phonon Coupling", *Physical Review B*, Vol. 101, No. 11, pp. 1–8, 2020.

44. Bertolazzi, S., J. Brivio and A. Kis, "Stretching and Breaking of Ultrathin MoS_2", *ACS Nano*, Vol. 5, No. 12, pp. 9703–9709, 2011.

45. Desai, S. B., G. Seol, J. S. Kang, H. Fang, C. Battaglia, R. Kapadia, J. W. Ager, J. Guo and A. Javey, "Strain-Induced Indirect to Direct Bandgap Transition in Multilayer WSe_2", *Nano Letters*, Vol. 14, No. 8, pp. 4592–4597, 2014.

46. Yu, Y., C.-D. Dong, R. Binder, S. Schumacher and C.-Z. Ning, "Strain-Induced Indirect-to-Direct Bandgap Transition, Photoluminescence Enhancement, and Linewidth Reduction in Bilayer $MoTe_2$", *ACS Nano*, Vol. 17, No. 5, pp. 4230–4238, 2023.

47. Wang, F., S. Li, M. A. Bissett, I. A. Kinloch, Z. Li and R. J. Young, "Strain Engineering in Monolayer WS_2 and WS_2 Nanocomposites", *2D Materials*, Vol. 7, No. 4, pp. 1–13, 2020.

48. Schmidt, R., I. Niehues, R. Schneider, M. Drüppel, T. Deilmann, M. Rohlfing, S. M. de Vasconcellos, A. Castellanos-Gomez and R. Bratschitsch, "Reversible Uniaxial Strain Tuning in Atomically Thin WSe_2", *2D Materials*, Vol. 3, No. 2, pp. 1–7, 2016.

49. Di Giorgio, C., E. Blundo, G. Pettinari, M. Felici, Y. Lu, A. M. Cucolo, A. Polimeni and F. Bobba, "Nanoscale Measurements of Elastic Properties and Hydrostatic Pressure in H2-Bulged MoS_2 Membranes", *Advanced Materials Interfaces*, Vol. 7, No. 23, pp. 1–11, 2020.

50. Frisenda, R., M. Drüppel, R. Schmidt, S. Michaelis de Vasconcellos, D. Perez de Lara, R. Bratschitsch, M. Rohlfing and A. Castellanos-Gomez, "Biaxial Strain Tuning of the Optical Properties of Single-Layer Transition Metal Dichalcogenides",

npj 2D Materials and Applications, Vol. 1, No. 1, pp. 1–7, 2017.

51. Yuan, L. and L. Huang, "Exciton Dynamics and Annihilation in WS_2 2D Semiconductors", *Nanoscale*, Vol. 7, No. 16, pp. 7402–7408, 2015.

52. Ye, Z., T. Cao, K. O'Brien, H. Zhu, X. Yin, Y. Wang, S. G. Louie and X. Zhang, "Probing Excitonic Dark States in Single-Layer Tungsten Disulphide", *Nature*, Vol. 513, No. 7517, pp. 214–218, 2014.

53. Wilson, J. and A. Yoffe, "The Transition Metal Dichalcogenides: Discussion and Interpretation of the Observed Optical, Electrical, and Structural Properties", *Advances in Physics*, Vol. 18, No. 73, pp. 193–335, 1969.

54. Zeng, H., G.-B. Liu, J. Dai, Y. Yan, B. Zhu, R. He, L. Xie, S. Xu, X. Chen, W. Yao and X. Cui, "Optical Signature of Symmetry Variations and Spin-Valley Coupling in Atomically Thin Tungsten Dichalcogenides", *Scientific reports*, Vol. 3, pp. 1–5, 2013.

55. Gutiérrez, H. R., N. Perea-López, A. L. Elías, A. Berkdemir, B. Wang, R. Lv, F. López-Urías, V. H. Crespi, H. Terrones and M. Terrones, "Extraordinary Room-Temperature Photoluminescence in Triangular WS_2 Monolayers", *Nano Letters*, Vol. 13, No. 8, pp. 3447–3454, 2013.

56. Khatibi, Z., M. Feierabend, M. Selig, S. Brem, C. Linderälv, P. Erhart and E. Malic, "Impact of Strain on the Excitonic Linewidth in Transition Metal Dichalcogenides", *2D Materials*, Vol. 6, No. 1, pp. 1–9, 2018.

57. Plechinger, G., P. Nagler, J. Kraus, N. Paradiso, C. Strunk, C. Schüller and T. Korn, "Identification of Excitons, Trions, and Biexcitons in Single-Layer WS_2", *Physica Status Solidi Rapid Research Letters*, Vol. 9, No. 8, pp. 457–461, 2015.

58. Palacios-Berraquero, C., D. M. Kara, A. R. P. Montblanch, M. Barbone, P. Latawiec, D. Yoon, A. K. Ott, M. Loncar, A. C. Ferrari and M. Atatüre, "Large-Scale

Quantum-Emitter Arrays in Atomically Thin Semiconductors", *Nature Communications*, Vol. 8, No. 1, pp. 1–6, 2017.

59. Flatten, L. C., Z. He, D. M. Coles, A. A. P. Trichet, A. W. Powell, R. A. Taylor, J. H. Warner and J. M. Smith, "Room-Temperature Exciton-Polaritons with Two-Dimensional WS_2", *Scientific Reports*, Vol. 6, No. 1, pp. 1–7, 2016.

60. Ye, Y., Z. J. Wong, X. Lu, X. Ni, H. Zhu, X. Chen, Y. Wang and X. Zhang, "Monolayer Excitonic Laser", *Nature Photonics*, Vol. 9, No. 11, pp. 733–737, 2015.

61. Li, Y., A. Chernikov, X. Zhang, A. Rigosi, H. M. Hill, A. M. van der Zande, D. A. Chenet, E.-M. Shih, J. Hone and T. F. Heinz, "Measurement of the Optical Dielectric Function of Monolayer Transition-Metal Dichalcogenides: MoS_2, $MoSe_2$, WS_2, and WSe_2", *Physical Review B*, Vol. 90, No. 20, pp. 1–6, 2014.

62. Katzer, M., S. Kovalchuk, K. Greben, K. I. Bolotin, M. Selig and A. Knorr, "Impact of Dark Excitons on Förster-Type Resonant Energy Transfer Between Dye Molecules and Atomically Thin Semiconductors", *Physical Review B*, Vol. 107, No. 3, pp. 1–15, 2023.

63. Prins, F., A. J. Goodman and W. A. Tisdale, "Reduced Dielectric Screening and Enhanced Energy Transfer in Single- and Few-Layer MoS_2", *Nano Letters*, Vol. 14, No. 11, pp. 6087–6091, 2014.

64. Swathi, R. S. and K. L. Sebastian, "Long-Range Resonance Energy Transfer from a Dye Molecule to Graphene Has (Distance)$^{-4}$ Dependence", *the Journal of Chemical Physics*, Vol. 30, No. 8, pp. 1–4, 2009.

65. Gordon, J. M. and Y. N. Gartstein, "Dielectric Polarization, Anisotropy and Nonradiative Energy Transfer into Nanometre-scale Thin Semiconducting Films", *Journal of Physics Condensed Matter*, Vol. 25, No. 42, pp. 1–10, 2013.

66. Raja, A., A. MontoyoCastillo, J. Zultak, X. Zhang, Z. Ye, C. Roquelet, D. A.

Chenet, A. M. van der Zande, P. Huang, S. Jockusch, J. Hone, D. R. Reichman, L. E. Brus and T. F. Heinz, "Energy Transfer from Quantum Dots to Graphene and MoS_2:The Role of Absorption and Screening in Two-Dimensional Materials", *Nano Letters*, Vol. 16, No. 4, pp. 2328–2333, 2016.

67. Aslan, B., C. Yule, Y. Yu, Y. J. Lee, T. F. Heinz, L. Cao and M. L. Brongersma, "Excitons in Strained and Suspended Monolayer WSe_2", *2D Materials*, Vol. 9, No. 1, pp. 1–12, 2022.

68. Deng, S., A. V. Sumant and V. Berry, "Strain Engineering in Two-Dimensional Nanomaterials Beyond Graphene", *Nano Today*, Vol. 22, pp. 14–35, 2018.

69. Verre, R., D. G. Baranov, B. Munkhbat, J. Cuadra, M. Käll and T. Shegai, "Transition Metal Dichalcogenide Nanodisks as High-Index Dielectric Mie Nanoresonators", *Nature Nanotechnology*, Vol. 14, No. 7, pp. 679–683, 2019.

70. Frasco, M. F. and N. Chaniotakis, "Semiconductor Quantum Dots in Chemical Sensors and Biosensors", *Sensors*, Vol. 9, No. 9, pp. 7266–7286, 2009.

71. Schneider, C. A., W. S. Rasband and K. W. Eliceiri, "NIH Image to ImageJ: 25 Years of Image Analysis", *Nature Methods*, Vol. 9, No. 7, pp. 671–675, 2012.

72. Dabbousi, B. O., J. Rodriguez-Viejo, F. V. Mikulec, J. R. Heine, H. Mattoussi, R. Ober, K. F. Jensen and M. G. Bawendi, "(CdSe)ZnS Core-Shell Quantum Dots: Synthesis and Characterization of a Size Series of Highly Luminescent Nanocrystallites", *The Journal of Physical Chemistry B*, Vol. 101, No. 46, pp. 9463–9475, 1997.

73. Kristensen, P. T., J. E. Mortensen, P. Lodahl and S. Stobbe, "Shell Theorem for Spontaneous Emission", *Physical Review B*, Vol. 88, No. 20, pp. 1–5, 2013.

74. Kramers, H. A., "La Diffusion de La Lumière par Les Atomes", *Atti del Congresso Internazionale dei Fisici*, pp. 545–557, Bologna, Italy, 1924.

75. de Kronig, R., "On the Theory of Dispersion of X-rays", *Journal of the Optical Society of America*, Vol. 12, pp. 547–557, 1926.

76. Kuzmenko, A. B., "Kramers–Kronig Constrained Variational Analysis of Optical Spectra", *Review of Scientific Instruments*, Vol. 76, No. 8, pp. 83–108, 2005.

77. Dressel, M. and G. Grüner, *Electrodynamics of Solids*, Cambridge University Press, Cambridge, U.K., 2002.

78. Lucovsky, G., R. M. White, J. A. Benda and J. F. Revelli, "New Valence Force Model for Diamond-Structure Solids", *Physical Review B*, Vol. 7, No. 8, pp. 3859–3870, 1973.

79. Radisavljevic, B., A. Radenovic, J. Brivio, V. Giacometti and A. Kis, "Single-Layer MoS_2 Transistors", *Nature Nanotechnology*, Vol. 6, pp. 147–150, 2011.

80. Beal, A. R., W. Y. Liang and H. P. Hughes, "Kramers-Kronig Analysis of the Reflectivity Spectra of 3R-WS_2 and 2H-WSe_2", *Journal of Physics C: Solid State Physics*, Vol. 9, No. 12, pp. 2449–2457, 1976.

81. Liu, F., "Mechanical Exfoliation of Large Area 2D Materials from VdW Crystals", *Progress in Surface Science*, Vol. 96, No. 2, pp. 1–17, 2021.

82. Carrascoso, F., H. Li, R. Frisenda and A. Castellanos-Gomez, "Strain Engineering in Single-, Bi-, and Tri-Layer MoS_2, $MoSe_2$, WS_2, and WSe_2", *Nano Research*, Vol. 14, No. 6, pp. 1698–1703, 2021.

83. van de Groep, J., Q. Li, J.-H. Song, P. G. Kik and M. L. Brongersma, "Impact of Substrates and Quantum Effects on Exciton Line Shapes of 2D Semiconductors at Room Temperature", *Nanophotonics*, Vol. 12, No. 16, pp. 3291–3300, 2023.

84. Yu, Y., Y. Yu, C. Xu, A. Barrette, K. Gundogdu and L. Cao, "Fundamental Limits of Exciton-Exciton Annihilation for Light Emission in Transition Metal

Dichalcogenide Monolayers", *Physical Review B*, Vol. 93, No. 20, pp. 1–5, 2016.

85. Chaste, J., A. Missaoui, S. Huang, H. Henck, Z. Ben Aziza, L. Ferlazzo, C. Naylor, A. Balan, A. T. C. J. Johnson, R. Braive and A. Ouerghi, "Intrinsic Properties of Suspended MoS_2 on SiO_2/Si Pillar Arrays for Nanomechanics and Optics", *ACS Nano*, Vol. 12, No. 4, pp. 3235–3242, 2018.

86. Tanoh, A. O. A., N. Gauriot, G. Delport, J. Xiao, R. Pandya, J. Sung, J. Allardice, Z. Li, C. A. Williams, A. Baldwin, S. D. Stranks and A. Rao, "Directed Energy Transfer from Monolayer WS_2 to Near-Infrared Emitting PbS-CdS Quantum Dots", *ACS Nano*, Vol. 14, No. 11, pp. 15374–15384, 2020.

87. Prasai, D., A. R. Klots, A. Newaz, J. S. Niezgoda, N. J. Orfield, C. A. Escobar, A. Wynn, A. Efimov, G. K. Jennings, S. J. Rosenthal and K. I. Bolotin, "Electrical Control of Near-Field Energy Transfer Between Quantum Dots and Two-Dimensional Semiconductors", *Nano Letters*, Vol. 15, No. 7, pp. 4374–4380, 2015.

88. Li, J., W. Zhang, Y. Zhang, H. Lei and B. Li, "Temperature-Dependent Resonance Energy Transfer from CdSe–ZnS Core–Shell Quantum Dots to Monolayer MoS_2", *Nano Research*, Vol. 9, No. 9, pp. 2623–2631, 2016.

89. Kim, M. M., Y. Huang, K. Choi and C. H. Hidrovo, "The Improved Resistance of PDMS to Pressure-Induced Deformation and Chemical Solvent Swelling for Microfluidic Devices", *Microelectronic Engineering*, Vol. 124, pp. 66–75, 2014.

90. Cong, C., J. Shang, Y. Wang and T. Yu, "Optical Properties of 2D Semiconductor WS_2", *Advanced Optical Materials*, Vol. 6, No. 1, pp. 1–15, 2018.

91. Salapare III, H., F. Guittard, H. S. Cosiñero, B. Suarez, M. Bacaoco, J. Nuñez and H. Ramos, "Plasma Surface Modification of PETG Sheets for Enhanced Adhesion Performance", *Joint 13th Asia Pacific Physics Conference and 22nd Australian*

Institute of Physics Congress, p. 1, Brisbane, Australia, 2016.

92. Perez-Roldan, M. J., D. Debarnot and F. Poncin-Epaillard, "Processing of Plasma-Modified and Polymer-Grafted Hydrophilic PET surfaces, and Study of Their Aging and Bioadhesive Properties", *RSC Advances*, Vol. 4, No. 59, pp. 31409–31415, 2014.

93. Joensen, P., R. F. Frindt and S. R. Morrison, "Single-Layer MoS_2", *Materials Research Bulletin*, Vol. 21, No. 4, pp. 457–461, 1986.

94. Liu, K. C. and T. F. George, "Spontaneous Emission by Two Atoms with Different Resonance Frequencies Near a Metal Surface", *Physical Review B*, Vol. 32, No. 6, pp. 3622–3633, 1985.

95. Najmaei, S., Z. Liu, W. Zhou, X. Zou, G. Shi, S. Lei, B. I. Yakobson, J.-C. Idrobo, P. M. Ajayan and J. Lou, "Vapour Phase Growth and Grain Boundary Structure of Molybdenum Disulphide Atomic Layers", *Nano Letters*, Vol. 13, No. 8, pp. 3876–3880, 2013.

96. Niehues, I., R. Schmidt, M. Drüppel, P. Marauhn, D. Christiansen, M. Selig, G. Berghäuser, D. Wigger, R. Schneider, L. Braasch, R. Koch, A. Castellanos-Gomez, T. Kuhn, A. Knorr, E. Malic, M. Rohlfing, S. Michaelis De Vasconcellos and R. Bratschitsch, "Strain Control of Exciton-Phonon Coupling in Atomically Thin Semiconductors", *Nano Letters*, Vol. 18, No. 3, pp. 1751–1757, 2018.

97. Mirshojaeian Hosseini, M. J. and R. A. Nawrocki, "A Review of the Progress of Thin-Film Transistors and Their Technologies for Flexible Electronics", *Micromachines*, Vol. 12, No. 6, pp. 1–19, 2021.

98. Wang, Q. and D. Kong, "Transition-Metal Doped Atomically Thin MoS_2 Layers", *Advanced Optical Materials*, Vol. 4, pp. 1–8, 2016.

APPENDIX A: FIGURE LICENCES

Figure 1.2 is reproduced with permission from Springer Nature under license number 5875391506195.

Figure 1.3 is reprinted with permission from Won Seok Yun, S. W. Han, Soon Cheol Hong, In Gee Kim, and J. D. Lee, Phys. Rev. B 85, 033305 (2012), under license number RNP/24/SEP/083699. Copyright 2012 by the American Physical Society.

Figure 1.5 is in the public domain and has been reprinted (adapted) with permission from Nano Letters 2014, 14(8), 4592-4597. Copyright 2014 by the American Chemical Society.

Figure 7.6 is in the public domain and has been reprinted (adapted) with permission from Nano Letters 2016, 16(4), 2328-2333. Copyright 2016 by the American Chemical Society.

Figures 1.4 and 1.4 are available under a Creative Commons License and do not require permission for reuse.